CO_2 increase experiments using the Community Earth System Model (CESM): Relationship to climate sensitivity and comparison of CESM1 to CESM2

J. T. Bacmeister, C. Hannay, B. Medeiros, A. Gettelman, R. Neale, H. B. Fredriksen, W. H. Lipscomb, I. Simpson, D. A. Bailey, M. Holland, K. Lindsay, B. Otto-Bliesner

Key Points:

- Climate sensitivity has increased from 4K to over 5K in CESM2 compared to CESM1.
- Shortwave radiation feedbacks over the Southern Ocean play a key role in determining the response of CESM to increasing CO_2.
- Various measures of climate response, including equilibrium climate sensitivity (ECS) and transient climate response (TCR) are not simply related in CESM.

Abstract

We examine the response of the Community Earth System Model versions 1 and 2 (CESM1 and CESM2) to abrupt quadrupling of atmospheric CO_2 concentrations (4xCO2) and to 1% annually increasing CO_2 concentrations (1%CO2). Different estimates of equilibrium climate sensitivity (ECS) for CESM1 and CESM2 are presented. All estimates show that the sensitivity of CESM2 has increased by 1.5K or more over that of CESM1. At the same time the transient climate response (TCR) of CESM1 and CESM2 derived from 1%CO2 experiments has not changed significantly - 2.1K in CESM1 and 2.0K in CESM2. Increased initial forcing as well as stronger shortwave radiation feedbacks are responsible for the increase in ECS seen in CESM2. A decomposition of regional radiation feedbacks and their contribution to global feedbacks shows that the Southern Ocean plays a key role in the overall behavior of 4xCO2 experiments, accounting for about 50 % of the total shortwave feedback in both CESM1 and CESM2. The Southern Ocean is also responsible for around half of the increase in shortwave feedback between CESM1 and CESM2, with a comparable contribution arising over tropical ocean. Experiments using a thermodynamic slab-ocean model (SOM) yield estimates of ECS that are in remarkable agreement with those from fully-coupled earth system model (ESM) experiments for the same level of CO_2 increase. Finally, we show that the similarity of TCR in CESM1 and CESM2 masks significant regional differences in warming that occur in the 1%CO2 experiments for each model.

Plain Language Summary

Computer models of the earth's climate system are complex. Our best guess scenarios for how the climate system will change due to human activity over the next century are also complex. They include estimates of changing greenhouse gas (e.g. CO2) levels in the atmosphere, aerosol (e.g., smog, haze) emissions, and land-use changes (e.g., deforestation, urbanization). To help understand this complex system, the climate modeling community has designed two simplified experiments – "abrupt CO2 quadrupling" (4xCO2) and "one-percent annual CO2 increase" (1%CO2). In these experiments all human-induced factors in the climate system are held constant (at "pre-industrial levels") except for CO2 in the atmosphere. Results of these experiments from different climate models can be compared to gain insight into the climate system. We look at two versions of the Community Earth System Model (CESM1 and CESM2). The warming simulated in the 4xCO2 experiment ("climate sensitivity") has increased substantially in CESM2. This is related to changes in clouds over the Southern Ocean and tropics. At the same time warming in in the 1%CO2 experiment has not increased. This is related to differences in how CESM1 and CESM2 simulate northern oceans (Arctic, N. Atlantic and N. Pacific).

1 Introduction

The coupled climate system responds in complicated ways to anthropogenic changes in greenhouse gas concentrations, aerosol emissions, and land use, among other factors. To investigate climate model response to these forcings, two idealized configurations were introduced in the Coupled Model Intercomparison Project phase 5 (CMIP5; Taylor et al., 2012): 1) the abrupt 4xCO2 increase experiment; and 2) the 1%CO2 increase experiment. For both experiments, a fully-coupled atmosphere-ocean general circulation model (AOGCM) or Earth system model (ESM) is run to equilibrium using estimated pre-industrial (year≈1850) greenhouse gas concentrations, aerosol emissions, land use, and other climate forcings. The equilibrated pre-industrial control run (piCTL) is then subjected to an abrupt quadrupling of atmospheric CO_2, or to 1% annually-increasing CO_2, while holding all other forcings at pre-industrial levels. Both experiments are part of the initial Diagnostic, Evaluation and Characterization of Klima (DECK) requirements for partici-

pation in Phase 6 of the Coupled Model Intercomparison Project (CMIP6; Eyring et al., 2016).

Table 1. Measures of climate response discussed in this analysis. All values in degrees Kelvin (K). SOM-based numbers for CESM1 equilibrium climate sensitivity (ECS-SOM; 1st row, 1st column) are taken from Gettelman et al. (2012). Two numbers given are for 1° and 2° horizontal resolutions respectively. All other numbers were calculated for this study. Details of the calculations are given in Appendix A. Second column shows ECS-SOM(4x) based on SOM runs subject to a 4xCO2 increase (Section 5). Inferred ECS (iECS; 3rd and 4th columns) is derived from linear regression analysis of $\overline{\mathcal{N}}(\Delta\overline{T})$ from abrupt CO2 increase experiments (Gregory et al., 2004). Transient climate response (TCR; 5th column) is derived from experiments subject to a 1% annual CO2 increase (Section 6). Standard errors, where available, are shown in parentheses.

Equilibrium Climate Sensitivity based on 2xCO2 SOM experiments (ECS-SOM)	ECS-SOM(4x) based on 4xCO2 SOM experiments	Inferred ECS (iECS) based on 150-year regression	iECS based on 800 years	Transient Climate Response (TCR)
		CESM1		
4.0, 4.2	4.2(0.03)	3.4(0.04)	4.2(0.05)	2.1(0.07)
		CESM2		
5.5(0.03)	6.5(0.07)	5.3(0.22)	6.5(0.07)	2.0(0.04)

Equilibrium Climate Sensitivity (ECS) is defined as the equilibrium warming that would occur under a doubling of CO_2 (Charney et al., 1979). The abrupt 4xCO2 increase scenario was introduced to evaluate model climate sensitivity. The CMIP 4xCO2 experimental design calls for 150 years of simulation, although the long oceanic timescales in the climate system imply that coupled simulations may require ∼1000 years to reach a new equilibrium (e.g., Danabasoglu & Gent, 2009; Rugenstein et al., 2019). ECS has been estimated from 4xCO2 experiments using linear regression to global mean top-of-atmosphere (or top-of-model) radiative imbalance $\overline{\mathcal{N}}$ and global mean warming $\Delta\overline{T}$ (Gregory et al., 2004). The linear fit to $\overline{\mathcal{N}}(\Delta\overline{T})$ is extrapolated to $\overline{\mathcal{N}} = 0$ to estimate an equilibrium warming $\Delta\overline{T}_{eq}$, which is divided by 2 (under the assumption of linearity) to estimate ECS. We will refer to the ECS estimate derived in this way as the inferred ECS or iECS. The iECS approach was applied to 150-year 4xCO2 AOGCM/ESM simulations to derive the published ECS values for CMIP5 (Flato et al., 2014).

Another approach to estimating ECS was proposed by Danabasoglu and Gent (2009), using a thermodynamic slab-ocean model (SOM) rather than a full dynamical ocean in abrupt CO_2 increase experiments to eliminate the long timescales produced by the slow deep-ocean responses to warming. The SOM experiments equilibrate in decades rather than centuries, yielding a SOM-based estimate of ECS (ECS-SOM).

Both the iECS and ECS-SOM approaches to estimating the true ECS of a coupled model have shortcomings. A drawback of the iECS approach is that $\overline{\mathcal{N}}(\Delta\overline{T})$ may be a nonlinear function of $\Delta\overline{T}$, leading to iECS values that depend on the number of years in the regression analysis (e.g.; Williams et al., 2008; Andrews et al., 2012). The radiative response to abrupt CO_2 increase is also known to be nonlinear (e.g.; Etminan et al., 2016). In the case of ECS-SOM, it is unclear whether details in the construction of a SOM configuration can affect the resulting ECS (e.g.; Stouffer & Manabe, 1999; Senior & Mitchell, 2000; Williams et al., 2008; Danabasoglu & Gent, 2009).

Table 1 gives values of ECS-SOM, iECS, and transient climate response (TCR; Taylor et al., 2012) for two versions of the Community Earth System Model (CESM). All

estimates of ECS have increased substantially in version 2 of CESM (CESM2; Danabasoglu et al., 2020). ECS-SOM has increased by over 1K compared to its predecessor, with values of 5.4K in CESM2 (Gettelman, Hannay, et al., 2019) compared to 4.0K (1° resolution) or 4.2K (2° resolution) in CESM1 (Gettelman et al., 2012). These ECS-SOM values were derived from SOM experiments with 2xCO2 forcing (Danabasoglu & Gent, 2009; Gettelman, Hannay, et al., 2019).

Figure 1 illustrates key features of 4xCO2 experiments using CESM1 and CESM2. Fig. 1a shows global mean top-of-model radiative imbalance $\overline{\mathcal{N}}$ as a function of global mean surface temperature $\Delta\overline{T}$ for CESM1 (black) and CESM2 (red). The equilibrium temperature of the respective piCTL simulation (Table 2) has been subtracted from $\overline{T}$ to give $\Delta\overline{T}$. Although the fully-coupled 4xCO2 runs shown in Fig. 1a are over 800 years in length, they have not equilibrated. Also, we see that $\overline{\mathcal{N}}(\Delta\overline{T})$ for both CESM1 and CESM2 exhibits nonlinearity (e.g;. Andrews et al., 2012), i.e., a change in the slope of $\overline{\mathcal{N}}(\Delta\overline{T})$ with warming. The presence of such nonlinearity has been attributed to rapid nonlinear low-cloud SST feedbacks (Williams et al., 2008) and multiple timescales of deep-ocean heat uptake (e.g.; Senior & Mitchell, 2000; Held et al., 2010; Li et al., 2013).

Fig. 1b shows ECS inferred from linear regressions (iECS) of $\overline{\mathcal{N}}$ versus $\Delta\overline{T}$ as a function of years used in the regression. Not only has the magnitude of iECS changed between CESM1 and CESM2, but the time evolution of iECS has also changed. CESM1 exhibits a long initial period ($\sim$150 year) during which iECS is relatively constant near 3.5K, or even weakly decreasing, before increasing to values slightly over 4K by year 800. In CESM2, however, iECS increases rapidly from year 20 onwards and quickly exceeds the published ECS of 5.4K (Gettelman, Hannay, et al., 2019) between years 150 and 200. The iECS for CESM1 derived from the full 150 years of the prescribed 4xCO2 experiment is around 3.4K, well below the value derived from SOM runs or from longer periods of the 4xCO2 run. In CESM2, the iECS in year 150 is around 5.5K, but approaches 6.5K as more years are used in the regression. In Section 5 we will show that the iECS at long times agrees with ECS-SOM with 4xCO2 forcing for both CESM1 and CESM2.

Figs. 1c and d show timeseries of $\overline{T}$ for CESM1 and CESM2, again with interesting differences between the two models. In CESM1 an extended pause (hiatus) in warming sets in after a short initial period of rapid warming. The hiatus lasts for around 100 years, after which gradual warming resumes. Warming in CESM2 has no such hiatus; rates of warming decrease consistently over the integration. The warming hiatus in CESM1 appears to be the ultimate cause of the local minimum in iECS around year 100 (Fig. 1b).

A second frequently used measure of climate model response to CO_2 forcing is the transient climate response (TCR), defined as the global mean warming averaged over years 60–80 in the 1%CO2 experiment with respect to piCTL. As shown in Table 1, TCR values have changed little between CESM1 (2.1K) and CESM2 (2.0K) despite the large changes in ECS.

In the remainder of this paper we will address three topics: 1) the increase in climate sensitivity between CESM1 and CESM2; 2) the relationship between SOM-based estimates of ECS and those from fully-coupled ESM runs using a dynamic ocean; and 3) the behavior of the 1%CO2 configurations of CESM1 and CESM2 and its relation to TCR. We find that the increased climate sensitivity of CESM2 arises from both stronger shortwave radiation feedbacks with surface temperature T_s and from increased initial forcing $\overline{\mathcal{N}}_0$. The strengthened shortwave feedbacks in CESM2 originate primarily in low-cloud feedbacks over the Southern Ocean and in tropical high-cloud feedbacks. We find that SOM-based estimates of ECS agree with those based on full ESM simulations, despite differences in regional warming patterns. We will also see that 1%CO2 experiments for CESM1 and CESM2 differ more than is implied by the similar values of TCR. In particular, TCR does not capture significant regional variations between the models.

Table 2. Equilibrium parameters from pre-industrial control (piCTL) experiments. These values are calculated from 150 year means following the initial year of the 1%CO2 and 4xCO2 experiments.

Global Mean Surface Temperature	Global Mean Top-of-model Radiation fluxes
CESM1	
287.2K	235.0 Wm^{-2}
CESM2	
288.3K	239.2 Wm^{-2}

The paper is organized as follows: Section 2 briefly describes CESM1, CESM2, the CESM Slab Ocean Model, and the experimental set-ups used in this study. A notable feature of this study is a comparison of fully-coupled 4xCO2 ESM integrations with 4xCO2 SOM integrations. Section 3 details the model variables examined and describes analysis methods, including a consistent treatment of regional versus global feedback parameters. Section 4 describes results from the fully-coupled 4xCO2 experiments, including analysis of longwave and shortwave radiative responses (Section 4.1), regional decomposition of feedbacks (Section 4.3), and an analysis of cloud responses (Section 4.4). Section 5 describes SOM-based abrupt CO_2 increase experiments and compares them with full ESM results. Section 6 examines results from 1%CO2 experiments using CESM1 and CESM2. Finally, Section 7 summarizes our results and discusses implications of the various measures of climate response.

2 Models and Experimental Design

2.1 CESM2 and CESM1

The Community Earth System Model version 2 (CESM2; Danabasoglu et al., 2020) was developed over five years for participation in CMIP6 (Eyring et al., 2016). This development was finished in December 2018, and CMIP6 DECK simulations with CESM2 are now complete. Its predecessor model, CESM1 (Hurrell et al., 2013), has been extensively documented. The versions of CESM1 examined here are those used in the Last-millenium ensemble project (LME; Otto-Bliesner et al., 2016) and the CESM Large Ensemble project (LENS; Kay et al., 2015). The only differences between these versions are the atmospheric horizontal resolution, 2° for LME and 1° for LENS, as well as some retuning of low-cloud fraction. Results of the pre-industrial and 20th century historical simulations using the LME version of CESM1 were contributed to the CMIP5 archive as "CESM1(CAM5.1, FV2)".

CESM2 incorporated major changes to several component models, including atmosphere, land, and ocean. A new interactive model of the Greenland Ice Sheet (Lipscomb et al., 2019) was also introduced. (Ice sheet elevation and extent were held fixed, however, in the simulations analyzed here.) In addition to component development, emissions datasets and other forcing datasets were substantially revised for CMIP6 (Hoesly et al., 2018).

The CESM2 atmosphere component differs substantially from that in CESM1. Every physics parameterization, except for the rapid radiative transfer model for GCM applications (RRTMG; Iacono et al., 2008), was replaced or modified (Neale et al., 2020). The major physics changes relevant to cloud and turbulence processes are the replacement of shallow convection, boundary layer turbulence, and cloud macrophysics schemes in CESM1 with the Cloud Layers Unified by Binormals (CLUBB; Bogenschutz et al.,

Table 3. CESM experiments discussed in this analysis and their shorthand designations.

Designation	Model Version	Horiz. Res.	Setup	Length (years)
Fully-coupled, Earth System Model (ESM) runs				
CESM1-4xCO2	CESM1(LME)	2°	Abrupt 4xCO2 increase	800
CESM1b-4xCO2	CESM1(LENS)	1°	”	200
CESM2-4xCO2	CESM2.1	1°	”	1000
CESM1-1%CO2	CESM1(LME)	2°	1% annual CO2 increase	190
CESM2-1%CO2	CESM2.1	1°	1% annual CO2 increase	150
Slab-ocean model (SOM) runs				
CESM1b-4xCO2-SOM	CESM1(LENS)	1°	Abrupt 4xCO2 increase	30
CESM2-4xCO2-SOM	CESM2.0	1°	”	100
CESM2-2xCO2-SOM	CESM2.0	1°	Abrupt 2xCO2 incease	100

2013) scheme and an update of cloud microphysics from the Morrison-Gettelman scheme version 1 (MG1; Morrison & Gettelman, 2008) to MG2 (Gettelman et al., 2015).

CLUBB is a turbulence and shallow-convection scheme based on higher-order closure, employing 10 higher-order moments of subgrid vertical velocity w', temperature T', and total moisture q_t'. CLUBB also produces large-scale cloud fraction and partitions between condensed and vapor phase water. MG2 is a sophisticated two-moment cloud microphysics scheme that explicitly models the interactions between clouds and aerosols. MG2 extends MG1 by including prognostic equations for rain and snow in addition to cloud ice and liquid. MG2 also includes changes to the treatment of mixed phase ice nucleation that have led to increased amounts of super-cooled liquid in mixed phase clouds.

Updates to ocean, land, land-ice and sea-ice components in CESM2 are discussed by Danabasoglu et al. (2020) and references therein.

2.2 Experimental Design

Abrupt 4xCO2 and 1%CO2 increase experiments are branched from equilibrated, fully-coupled pre-industrial control (piCTL) experiments in which all forcing (e.g., aerosol emissions, greenhouse gases, and land-use) is fixed at estimated 1850 levels. A CESM piCTL run is considered equilibrated if top-of-model radiative imbalance $|\overline{\mathcal{N}}|$ <0.1 Wm^{-2} in a 20-year mean. The CESM1 and CESM2 piCTL experiments used to initialize the CO_2 increase experiments are each over 1150 years in length. The 4xCO2 and 1%CO2 scenarios were branched off in year 1000 of the CESM1 piCTL experiment and in year 501 of the CESM2 piCTL. Equilibrium radiative fluxes and temperatures for the piCTL runs are given in Table 2.

In the 4xCO2 scenario, atmospheric CO_2 is abruptly quadrupled after branching, and the climate is allowed to evolve freely. The typical evolution of such runs is illustrated in Figure 1. In 1%CO2 experiments, an annually compounding increase in atmospheric CO_2 is imposed after branching, with other forcing fixed to piCTL values. For the CESM2 experiments discussed here, radiatively active species other than CO_2, notably ozone, are specified from piCTL experiments using the high-top Whole Atmosphere Community Climate Model (WACCM; Gettelman, Mills, et al., 2019) with fully-interactive chemistry. This procedure is discussed in detail by Danabasoglu et al. (2020). Impacts of this procedure on the evolution of CO_2 increase scenarios using CESM are under investigation, but will not be discussed here.

Table 3 summarizes the experiments discussed in this paper. We examine results from the 4xCO2 experiment performed for CMIP6 (CESM2-4xCO2) as well as two 4xCO2 experiments using CESM1: CESM1-4xCO2, performed with the LME version at 2° hor-

izontal resolution; and CESM1b-4xCO2, performed with the LENS version at 1° horizontal resolution. As noted in the table, the CESM1-4xCO2 and CESM2-4xCO2 experiments are significantly longer that the 150 years requested in the CMIP protocol. As seen in Fig. 1, equilibration of 4xCO2 experiments may take ∼1000 years or longer. We also examine results from the CESM2 1%CO2 run performed for CMIP6 (CESM2-1%CO2 and from a CESM1-1%CO2 run performed with the LME version of CESM1.

2.2.1 Slab-Ocean Model (SOM) Experiments

We also conducted abrupt CO_2 increase experiments using the CESM Slab Ocean model (SOM). The CESM-SOM configuration relies on ocean parameters derived from equilibrated, pre-industrial control simulations, and is designed to reproduce the climate of the fully-coupled ESM configuration (Bitz et al., 2012). The parameters used by the SOM are 2D annual-mean estimates of ocean mixed layer depths along with 2D monthly heat flux anomalies to the deep ocean. These parameters are used to drive an interactive thermodynamic slab that is forced from above by atmospheric fluxes. By construction, the global-mean deep-ocean heat flux is identically zero. ECS estimates for CESM and predecessors using 2xCO2 SOM simulations have been reported in several studies (e.g., Danabasoglu & Gent, 2009; Bitz et al., 2012; Gettelman et al., 2012; Gettelman, Hannay, et al., 2019). Here we will examine both 4xCO2 and 2xCO2 SOM experiments with CESM to quantify nonlinearity in ECS estimates and to enable direct comparison with fully-coupled experiments.

In the following, we append "SOM" to any experiments using the slab-ocean configuration. Experiments using fully-coupled CESM do not normally have a descriptive suffix, e.g., "CESM2-4xCO2". If clarity is a concern, the latter are designated as "ESM" (Earth system model) experiments.

3 Model Output and Analysis Methods

The analyses presented here use monthly and annually-averaged output from CESM, including radiative fluxes, cloud condensates and surface temperature. We use top-of-model (TOM) radiation fluxes rather than estimated top-of-atmosphere (TOA) fluxes, and surface temperature T_s rather than 2-meter air temperatures T_{2m}. The results are not sensitive to the TOM vs. TOA distinction or the T_s vs. T_{2m} distinction. Throughout this analysis T will always refer to surface temperature T_s.

Net TOM shortwave and longwave fluxes are denoted by $\mathcal{S}$ and $\mathcal{L}$, respectively. The TOM radiative imbalance $\mathcal{N}$, already introduced in Figure 1, is simply

$$\mathcal{N} = \mathcal{S} - \mathcal{L}. \tag{1}$$

We follow the usual atmospheric convention of defining upward longwave radiation flux and downward shortwave flux as positive.

CESM atmospheric model output also includes shortwave and longwave cloud radiative effect (CRE) $\mathcal{S}_{cld}$ and $\mathcal{L}_{cld}$, as well as TOM clear sky fluxes $\mathcal{S}_{clr}$ and $\mathcal{L}_{clr}$. These are calculated directly in the CAM radiation scheme in each grid column and time step and are approximately related to all-sky fluxes by:

$$\mathcal{S} \approx \mathcal{S}_{clr} + \mathcal{S}_{cld} \tag{2a}$$

$$\mathcal{L} \approx \mathcal{L}_{clr} - \mathcal{L}_{cld} \tag{2b}$$

where a small residual ($\sim$0.05 Wm^{-2}) exists due the definition of CRE at TOA instead of TOM. CESM follows the usual sign conventions for CRE: Negative $\mathcal{S}_{cld}$ indicates reflection of shortwave radiation by clouds, and positive $\mathcal{L}_{cld}$ indicates downward longwave radiation from clouds.

We also examine simulated total cloud amount c from CESM. This is calculated using the random overlap assumption across 3 cloud macrolayers bounded by the surface, 700 hPa, 400 hPa, and 50 hPa. Within each cloud macrolayer a fraction is calculated using maximum-random cloud overlap. Finally, we will examine liquid and ice cloud condensate paths (LWP and IWP, g m^{-2}). An estimate of in-cloud condensate paths is calculated by dividing monthly grid means of LWP and IWP by the cloud amount c, i.e.,

$$\mathrm{LWP}^* = \frac{\mathrm{LWP}}{c} \tag{3a}$$

$$\mathrm{IWP}^* = \frac{\mathrm{IWP}}{c} \tag{3b}$$

3.1 Regional and global feedback parameters

Studies of climate sensitivity focus on feedback relationships of the form

$$\delta X = \lambda_X \delta T \tag{4}$$

where X is a flux or other quantity of interest, T is surface temperature, and λ_X is a feedback parameter (slope) that linearly relates changes in X and T. X and T may represent regional or global mean quantities (e.g., Armour et al., 2013). Below, we will establish quantitative relationships between regional feedbacks and global feedbacks. We will be primarily interested in feedbacks between radiative fluxes and temperatures.

The global mean of X can be written as a sum of regional means over N regions,

$$\overline{X} = \sum_k a_k X_k(T_k,\ \ldots\ ) \tag{5}$$

where X_k is the mean of X in region k, T_k is the regional mean surfce temperature, and a_k is the areal fraction of region k. Global means will be denoted by $\overline{()}$ throughout this analysis.

The regional means X_k on the RHS of Eq 5 may depend on variables other than the regional surface temperature, including surface temperatures in other regions, or other meteorological variables such as vertical velocity or stability. We will assess the functional relationships between regional quantities and regional surface temperature T_k by examining scatterplots. If compact relationships exist over a range of values, even if nonlinear, we assume we are justified in assuming a relationship $X_k \approx X_k(T_k)$.

The global feedback parameter $\overline{\lambda}_X$ between $\overline{X}$ and $\overline{T}$ can then be estimated from a sum of regional feedbacks according to:

$$\overline{\lambda}_X = \frac{\delta\overline{X}}{\delta\overline{T}} \approx \sum_k a_k\ \frac{\partial X_k}{\partial T_k}\ \frac{\partial T_k}{\partial \overline{T}} \tag{6}$$

We approximate the derivatives on the RHS of Eq. 6 with slope parameters from linear regressions of X_k vs. T_k and of T_k vs. $\overline{T}$. The linear regression slope of X_k vs. T_k is simply the regional feedback parameter for X in region k and will be denoted $\lambda_{X;k}$. The linear regression slope of T_k versus $\overline{T}$ is the regional warming rate divided by the global rate. This is the amplification factor for regional warming and will be denoted by A_k. With these approximations, we rewrite Eq. 6:

$$\overline{\lambda}_X = \frac{\delta\overline{X}}{\delta\overline{T}} \approx \sum_k a_k\ A_k\ \lambda_{X;k} \tag{7}$$

The global feedback parameter $\overline{\lambda}_X$ has thus been written as a weighted sum of local feedbacks $\lambda_{X;k}$. The validity of regional decomposition can be tested by comparing the sum

in Eq. 7 with an independent regression using global mean quantities. This will be shown in Section 4.3.

CESM1-4xCO2 has large interannual variability compared CESM2-4xCO2 (e.g. Fig. 1d), likely related to strong ENSO. This is associated with correlated sub-decadal variations in $\mathcal{S}$ and T that have small but significant effects on linear regression estimates of $\lambda_{\mathcal{S}}$. For the analysis of long-term regional feedbacks we apply a decadal average to model results. Decadal averaging has negligible impacts on the analysis of CESM2-4xCO2 results. Its impacts in the analysis of CESM1-4xCO2 are largely restricted to calcuation of shortwave feedbacks in the tropics, and will be discussed further in Section 4.

3.2 Approximate partial radiative perturbations

We will examine cloud contributions to shortwave radiative forcing using the approximate partial radiative perturbation approach (APRP; Taylor et al., 2007). APRP constructs an analog to the full shortwave radiation calculation in an atmospheric model using monthly fields of clear-sky and all-sky shortwave fluxes at TOM and at the surface, as well as monthly total cloud amounts. The result is a reconstructed planetary albedo $\mathcal{A}$ that depends on 7 parameters

$$\mathcal{A}(c, \alpha_{clr}, \alpha_{oc}, \mu_{clr}, \mu_{cld}, \gamma_{clr}, \gamma_{cld}) \tag{8}$$

where c again is total cloud amount; α_{clr} and α_{oc} are clear-sky and overcast surface albedos; μ_{clr} and μ_{cld} are clear-sky and cloudy-sky absorption coefficients; and γ_{clr} and γ_{cld} are clear-sky and cloudy-sky scattering coefficients. The albedo and net all-sky TOM shortwave flux $\mathcal{S}$ are related by:

$$\mathcal{S} = \mathcal{S}^{\downarrow}(1 - \mathcal{A}) \tag{9}$$

where $\mathcal{S}^{\downarrow}$ is the incoming shortwave radiation at TOM. The APRP method provides estimates of the albedos, and absorption and scattering coefficients as well as an analytical expression for $\mathcal{A}$ that can be used to calculate partial derivatives and quantify the impact of different processes on shortwave radiation in the atmosphere. Given the importance of high-latitude responses in warming climates (e.g., Kay et al., 2014), it is particularly important to distinguish the roles of surface and cloud processes in the overall feedback.

3.3 Rapid and long-term timescales

Several studies (e.g., Held et al., 2010) have noted the existence of multiple timescales in the adjustment of the coupled climate system to abrupt perturbations. The behavior of $\overline{\mathcal{N}}(\Delta\overline{T})$ shown in Fig. 1a suggests the existence of at least two phases in the evolution of CESM after an abrupt quadrupling of CO_2. There is an initial phase with rapid warming and steep negative slope in $\overline{\mathcal{N}}(\Delta\overline{T})$, followed by a slower adjustment with nearly constant but shallower negative slope in $\overline{\mathcal{N}}(\Delta\overline{T})$, that persists until the end of both 4xCO2 experiments. The time evolution of $\overline{T}$ in CESM1 includes a long pause in warming from years 20 to 100 (Figs. 1c and 1d). During this pause, there is little evolution of $\overline{\mathcal{N}}(\Delta\overline{T})$, with values of $\Delta\overline{T}$ and $\overline{\mathcal{N}}$ fluctuating around 5K and 2 Wm^{-2}, respectively. Then warming in CESM1 resumes, and $\overline{\mathcal{N}}(\Delta\overline{T})$ is approximately linear with a slope of about -0.6 $\mathrm{Wm}^{-2}\mathrm{K}^{-1}$. Based on this behavior, we identify years 1–20 as representative of the rapid initial adjustment of both 4xCO2 experiments.

Inflection points for $\overline{\mathcal{N}}(\Delta\overline{T})$ indicated in Fig. 1a are estimated by determining the intersection of the linear fits for years 1–20 (not shown) and years 100–800. The loci of the year 100–800 linear fits at year 100 are also shown. For simplicity, we choose years 100–800 to describe the long-term behavior of both experiments, even though the transition in the slope of $\overline{\mathcal{N}}(\Delta\overline{T})$ occurs earlier in CESM2-4xCO2.

Table 4. Initial radiative imbalance $\overline{\mathcal{N}}_0$ and rapid initial adjustments to longwave ($\Delta\overline{\mathcal{L}}_0$) and shortwave fluxes ($\Delta\overline{\mathcal{S}}_0$) in 4xCO2 experiments. Numbers are diagnosed from linear fits to $\overline{\mathcal{N}}$, $\overline{\mathcal{L}}$, and $\overline{\mathcal{S}}$ during years 1–20 of CESM1-4xCO2 and CESM2-4xCO2. Regression parameters are used to extrapolate $\overline{\mathcal{N}}$, $\overline{\mathcal{L}}$ and $\overline{\mathcal{S}}$ to the equilibrium $\overline{T}$ from the corresponding piCTL experiment (or equivalently to $\Delta\overline{T}$=0).

$\overline{\mathcal{N}}_0$ (Wm^{-2})	$\Delta\overline{\mathcal{L}}_0$ (Wm^{-2})	$\Delta\overline{\mathcal{S}}_0$ (Wm^{-2})
CESM1-4xCO2		
7.4	-7.6	-0.2
CESM2-4xCO2		
8.6	-7.6	1.0

We use linear regressions of $\overline{\mathcal{N}}$, $\overline{\mathcal{S}}$, and $\overline{\mathcal{L}}$ versus $\overline{T}$ over years 1–20 of the 4xCO2 experiments, extrapolated to their corresponding piCTL equilibrium $\overline{T}$ values (Table 2), to estimate initial radiative forcing $\overline{\mathcal{N}}_0$ and ultra-rapid longwave and shortwave adjustments $\Delta\mathcal{L}_0$ and $\Delta\mathcal{S}_0$, which are given in Table 4.

4 Results from 4xCO2 Experiments

Here we will examine results from the extended 4xCO2 experiments, focusing on processes that contribute to the increased climate sensitivity of CESM2 compared to that of CESM1. As described in Appendix A, iECS is derived from linear fits to $\overline{\mathcal{N}}(\Delta\overline{T})$. :

$$\text{iECS} = -0.5\frac{\overline{\mathcal{N}}_I}{\overline{\lambda}_{\mathcal{N}}}, \tag{10}$$

where $\overline{\mathcal{N}}_I$ and $\overline{\lambda}_{\mathcal{N}}$ are the intercept and slope of the linear fit, and the factor of 0.5 scales 4xCO2 results to a 2xCO2 scenario assuming linearity (see Appendix A). In physical terms, $\overline{\lambda}_{\mathcal{N}}$ is the net radiation feedback with respect to T and $\overline{\mathcal{N}}_I$ is an estimate of the initial radiative forcing (which is equal to $\overline{\mathcal{N}}_0$ defined previously, for a regression over years 1-20).

Nonlinearity in $\overline{\mathcal{N}}(\Delta\overline{T})$ means that the linear fit parameters $\overline{\lambda}_{\mathcal{N}}$ and $\overline{\mathcal{N}}_I$ (slope and intercept) will change with the number and range of years used in the regression. Nevertheless, Eq. 10 is a useful starting point to examine factors controlling climate sensitivity. We see that sensitivity increases both as $\overline{\mathcal{N}}_I$ increases, and as the magnitude of $\overline{\lambda}_{\mathcal{N}}$ decreases.

4.1 Shortwave and longwave contributions to feedback and initial forcing

Figure 2 shows net shortwave and longwave TOM radiation fluxes, $\overline{\mathcal{S}}$ and $\overline{\mathcal{L}}$, as functions of $\overline{T}$ for CESM1-4xCO2 (black) and CESM2-4xCO2 (red). Fig 2 also shows equilibrium conditions for the piCTL experiments, in which $\overline{\mathcal{S}}$ and $\overline{\mathcal{L}}$ are within 0.1 Wm^{-2} of each other. Tables 4 and 5 give values of $\overline{\mathcal{N}}_0$, $\Delta\mathcal{L}_0$, and $\Delta\mathcal{S}_0$ as well as feedback parameters (slopes) $\overline{\lambda}_{\mathcal{N}}$, $\overline{\lambda}_{\mathcal{S}}$, and $\overline{\lambda}_{\mathcal{L}}$.

When CO_2 is quadrupled, $\overline{\mathcal{L}}$ decreases rapidly by about 7.6 Wm^{-2} in both CESM1-4xCO2 and CESM2-4xCO2, while $\overline{\mathcal{S}}$ adjusts by +1 Wm^{-2} in CESM2-4xCO2 and around -0.2 Wm^{-2} in CESM1-4xCO2. This yields a larger net initial forcing $\overline{\mathcal{N}}_0$ of 8.6 Wm^{-2} in CESM2-4xCO2 than 7.4 Wm^{-2} in CESM1-4xCO2 (Table 4). So, increased initial forcing, arising from a larger shortwave adjustment, is one component of the increased sensitivity of CESM2.

Table 5. Global feedback parameters for shortwave flux $\overline{\lambda}_{\mathcal{S}}$, longwave flux $\overline{\lambda}_{\mathcal{L}}$, and net radiative imbalance $\overline{\lambda}_{\mathcal{N}}$ for CESM1-4xCO2 and CESM2-4xCO2. Note that since $\overline{\mathcal{N}}=\overline{\mathcal{S}}-\overline{\mathcal{L}}$, the fourth column is simply the difference of the second and third columns. Standard errors for the regression slopes are shown in parentheses. Results for regressions using decadally-averaged quantities are shown for CESM1-4xCO2. Decadal averaging has no effect on CESM2-4xCO2 results.

Years	$\overline{\lambda}_{\mathcal{S}}$ ($\mathrm{Wm^{-2}K^{-1}}$)	$\overline{\lambda}_{\mathcal{L}}$ ($\mathrm{Wm^{-2}K^{-1}}$)	$\overline{\lambda}_{\mathcal{N}}$ ($\mathrm{Wm^{-2}K^{-1}}$)
CESM1-4xCO2			
1-20	0.99(0.08)	2.05(0.04)	-1.06 (0.09)
100-800	1.23(0.02)	1.82(0.01)	-0.59 (0.02)
100-800(dec.)	1.32(0.02)	1.81(0.02)	-0.49 (0.02)
CESM2-4xCO2			
1-20	0.87(0.06)	2.01(0.03)	-1.15 (0.07)
100-800	1.50(0.01)	1.86(0.01)	-0.36 (0.01)

The overall behavior of $\overline{\mathcal{L}}(\overline{T})$ in Fig. 2 is quite similar in CESM1-4xCO2 and CESM2-4xCO2, despite a small offset of about 2 $\mathrm{Wm^{-2}}$. We have already seen that in both experiments there is an initial adjustment in $\overline{\mathcal{L}}$ of around -7.6 $\mathrm{Wm^{-2}}$. Table 5 shows that the longwave feedback parameters $\overline{\lambda}_{\mathcal{L}}$ are also similar; initially around 2 $\mathrm{Wm^{-2}K^{-1}}$ and becoming slightly smaller during years 100–800, 1.82 $\mathrm{Wm^{-2}K^{-1}}$ for CESM1-4xCO2 and 1.86 $\mathrm{Wm^{-2}K^{-1}}$ for CESM2-4xCO2.

The long-term value of $\overline{\lambda}_{\mathcal{S}}$ for CESM2-4xCO2 is 1.50 $\mathrm{Wm^{-2}K^{-1}}$, significantly higher than in CESM1-4xCO2 (1.23 $\mathrm{Wm^{-2}K^{-1}}$). This produces the increased sensitivity in CESM2 by reducing the magnitude of long-term $\overline{\lambda}_{\mathcal{N}}$ ($=\overline{\lambda}_{\mathcal{S}}-\overline{\lambda}_{\mathcal{L}}$) from -0.59 $\mathrm{Wm^{-2}}$ in CESM1-4xCO2 to -0.36 $\mathrm{Wm^{-2}}$ in CESM2-4xCO2 (Table 5), overwhelming the small increase in $\overline{\lambda}_{\mathcal{L}}$ from CESM1 to CESM2. Thus, both factors that can lead to increased iECS in CESM2, $\overline{\mathcal{N}}_0$ and $\overline{\lambda}_{\mathcal{N}}$, are modified through the shortwave component $\overline{\mathcal{S}}$. The stronger nonlinearities in $\overline{\mathcal{N}}(\Delta\overline{T})$ for CESM2 also emerge from $\overline{\mathcal{S}}$.

We estimate the impact on ECS of the 1.2 $\mathrm{Wm^{-2}}$ increase in $\overline{\mathcal{N}}_0$ between CESM1 and CESM2 using the year 100–800 linear fits shown in Fig. 1a. The linear fit values of $\overline{\mathcal{N}}(\Delta\overline{T})$ and $\Delta\overline{T}$ at year 100 are indicated in the figure. For CESM2-4xCO2 we have $\Delta\overline{T}(100)$=6.58K and $\overline{\mathcal{N}}_{lin}(100)$=2.55 $\mathrm{Wm^{-2}}$. Using a slope $\overline{\lambda}_{\mathcal{N}}$=-0.36 $\mathrm{Wm^{-2}K^{-1}}$ (Table 5), we calculate an equilibrium warming of $6.58+\frac{2.55}{0.36}\approx$13.7K, i.e., the x-intercept of the red dashed line in Fig 1a. Lowering $\overline{\mathcal{N}}_{lin}(100)$ by 1.2 to 1.35 $\mathrm{Wm^{-2}}$ would yield an adjusted equilibrium warming of $6.58+\frac{1.35}{0.36}\approx$10.3K, corresponding to a climate sensitivity of 5.15K. So, with $\overline{\lambda}_{\mathcal{N}}$ as given in Table 5, reducing $\overline{\mathcal{N}}_0$ for CESM2-4xCO2 to its value in CESM1-4xCO2 gives a substantial reduction in ECS, but would still yield a sensitivity larger than 5K.

For comparison, we calculate the ECS that CESM2 would have if the long-term, net radiative feedback in CESM2-4xCO2 had the same value as in CESM1-4xCO2, i.e., -0.59 $\mathrm{Wm^{-2}K^{-1}}$ instead of -0.36 $\mathrm{Wm^{-2}K^{-1}}$. From Fig. 1a, we see a slope change in $\overline{\mathcal{N}}$ near $\Delta\overline{T}$=5K for both CESM1-4xCO2 and CESM2-4xCO2. The value of the linear regression fit to $\overline{\mathcal{N}}$ at $\Delta\overline{T}$=5K for CESM2-4xCO2 is 3.1 $\mathrm{Wm^{-2}}$. If the slope of $\overline{\mathcal{N}}(\Delta\overline{T})$ in CESM2-4xCO2 were steepened to -0.59 $\mathrm{Wm^{-2}K^{-1}}$ at this point, there would be additional warming of about $\frac{3.1}{0.59}\approx$5.3K, yielding a total warming of 10.3K, again corresponding to an ECS of around 5.15K.

We have seen that increased initial shortwave radiative forcing and increased shortwave radiation feedbacks play comparable roles in the greater sensitivity of CESM2-4xCO2 relative to CESM1-4xCO2. An important question which we cannot address here is how these two components of the sensitivity would change in an abrupt 2xCO2 ESM exper-

iment. However, experiments with the CESM2-SOM configuration (Section 5) suggest that feedback strength $\overline{\lambda}_{\mathcal{N}}$ in 2xCO2 and 4xCO2 experiments is similar, while there is nonlinearity in $\overline{\mathcal{N}}_0$. This implies that radiation feedbacks rather than initial forcing are more critical in understanding the increased ECS in CESM

4.1.1 Impact of sub-decadal variability

Table 5 shows that decadal averaging has a small but appreciable impact on regression estimates of shortwave feedback in CESM1-4xCO2. We believe this impact arises because sub-decadal variations in $\mathcal{S}$ and T are negatively correlated over large areas of the tropical ocean in CESM1-4xCO2 (not shown). The origin of these correlated variations is not completely understood but is likely related to strong ENSO in the LME version of CESM1 (Stevenson et al., 2016; Otto-Bliesner et al., 2016). It is worth emphasizing that the difference between the estimates of $\overline{\lambda}_{\mathcal{S}}$ using decadal and annual averages is not a reflection of statistical uncertainty in either estimate.

We will not address high-frequency variability further in this study. However, it is clear that this variability could have impacts on calculations of iECS from 4xCO2 experiments in some models.

4.1.2 Spatial pattern of initial adjustments

Before turning to the analysis of radiation feedbacks, we briefly examine the spatial distribution of the initial shortwave radiation and cloud adjustments in CESM1-4xCO2 and CESM2-4xCO2 in Figure 3. This is accomplished by comparing the averages of $\mathcal{S}$ and c over years 1–20 of the 4xCO2 experiments with the corresponding 20 year averages in the piCTL experiments after the branch year. The differences between these averages are denoted by $\Delta\mathcal{S}_{I20}$ and Δc_{I20}. These quantities characterize the rapid adjustment of clouds and shortwave radiation flux after quadrupling CO_2. Figure 3 shows the change in these adjustments between CESM1 and CESM2 denoted by $\delta_{1\rightarrow 2}(\Delta\mathcal{S}_{I20})$ (Fig. 3a) and $\delta_{1\rightarrow 2}(\Delta c_{I20})$ (Fig. 3b).

The global mean of 1.15 Wm^{-2} for $\delta_{1\rightarrow 2}(\Delta\mathcal{S}_{I20})$ is close to the 1.2 Wm^{-2} net change in $\Delta\overline{\mathcal{S}_0}$ between CESM1-4xCO2 and CESM2-4xCO2 (Table 4). There is significant spatial variability in $\delta_{1\rightarrow 2}(\Delta\mathcal{S}_{I20})$ with strong positive values occurring primarily over subtropical stratus regions. These maxima coincide with minima in $\delta_{1\rightarrow 2}(\Delta c_{I20})$ suggesting that stratus decks in CESM2 experience stronger initial thinning when CO_2 is quadrupled than those in CESM1. Reasons for this behavior are not clear.

4.2 Global distribution of feedbacks

Figure 4 shows maps of long-term linear regression slopes of quantities involved in shortwave radiative feedback for years 100–800 in CESM1-4xCO2 and CESM2-4xCO2. The annual mean fields of $\mathcal{S}$ and T have been smoothed in time with a running 10-year window, and in space with an 8° rectangular lat-lon window, before performing the linear regression.

Figures 4a,b show regression slopes of $T(x, y)$ versus $\overline{T}$. This is a local amplification factor for warming, which we denote by $A(x, y)$ and is the gridpoint analog of A_k in Eq 7. Both CESM1-4xCO2 and CESM2-4xCO2 exhibit polar amplification in both northern and southern high latitudes, although relative warming in the Arctic is much stronger in CESM1. This is likely related to differences in sea ice, as will be shown below. With the exception of the Arctic in CESM1-4xCO2, warming in both models is generally stronger in the southern hemisphere than in the north. Both models show weak warming $A(x, y)$ <0.5 in the northwest Atlantic, accompanied by similarly weak warm-

ing in the northwest Pacific in CESM1-4xCO2. An El Niño-like warming pattern is present in the equatorial and southeastern Pacific.

Figures 4c,d show regression slopes of $\mathcal{S}(x,y)$ versus local $T(x,y)$. This is the local feedback between shortwave radiation and surface temperature, which we denote by $\lambda_{\mathcal{S}}(x,y)$ and is the gridpoint analog of $\lambda_{\mathcal{S};k}$ in Eq 7. Despite the substantial changes in boundary layer and cloud physics parameterizations between CESM1 and CESM2, there are rough similarities in $\lambda_{\mathcal{S}}(x,y)$, particularly where low clouds are likely to control the shortwave response. Positive slopes with values between 3 and 5 $\mathrm{Wm^{-2}K^{-1}}$ are evident in the midlatitude storm tracks (NH and SH) and stratus/stratocumulus regions of both models. This suggests the presence of positive low-cloud SW feedbacks (i.e., thinner low clouds with higher T) of comparable magnitudes in both models. Shortwave feedbacks over the Southern Ocean stormtracks, however, are stronger in CESM2-4xCO2 by about 1 $\mathrm{Wm^{-2}K^{-1}}$. Also, CESM2-4xCO2 has a large $\lambda_{\mathcal{S}}(x,y)$ in the deep convective region over the western tropical Pacific, whereas this strong positive feedback (>5 $\mathrm{Wm^{-2}K^{-1}}$) is absent in CESM1.

Figures 4e,f show regression slopes of $\mathcal{S}(x,y)$ versus $\overline{T}$ in CESM1-4xCO2 and CESM2-4xCO2. Although the direct physical meaning of this regression quantity is unclear, this quantity is of interest since simple area integrals give the global feedback $\overline{\lambda}_{\mathcal{S}}$ (Andrews et al., 2015). Figures 4g,h show $\lambda_{\mathcal{S}}(x,y)\times A(x,y)$. This quantity should be close to the regression slopes of $\mathcal{S}$ versus $\overline{T}$ shown in Figs. 4e,f, and this is in fact the case. The agreement between Figs. 4e,f and Figs. 4g,h argues that regional feedbacks on decadal timescales and ∼8° spatial scales can be accurately decomposed according to Eqs. 6–7.

In addition, comparison of Figs. 4e,f or Figs. 4g,h with Figs. 4c,d highlights the role of regional warming in modulating the global shortwave feedback. In particular, the relatively strong warming of the Southern Ocean amplifies its contribution to the global shortwave feedback, while weak warming in the tropics reduces the contribution.

4.3 Regional feedbacks and their contribution to global climate sensitivity

Figure 5 shows regions that have been selected to examine regional radiation feedbacks: a) Arctic Ocean; b) N. Atlantic and N. Pacific north of 30°N (NAtlPac); c) Tropical Oceans between 30°S and 30°N (Trop_Ocn); d) mid-latitude Southern Ocean between 30°S and 60°S (SHml_Ocn); e) high-latitude Southern Ocean south of 60°S (SHhl_Ocn); f) Land north of 30°N (NH_Land); g) Tropical Land between 30°S and 30°N (Trop_Land); h) Land south of 30°S (SH_Land); and i) Global. The fractional global area of each region is shown in the panels. The N. Atlantic/N. Pacific and mid-latitude Southern Ocean regions (Figs. 5b,d) are chosen to characterize generally ice-free midlatitude oceans, while Arctic and high-latitude Southern Ocean regions (Figs. 5a,e) characterize high-latitude oceans in which sea-ice feedbacks may play a role.

Figure 6 shows timeseries of T in the analysis regions. After a rapid initial warming, there is a pause in warming, or even cooling, for about 100 years in the Arctic, N. Atlantic/N. Pacific and northern land regions (Figs. 6a,b,f) in both CESM1-4xCO2 and CESM2-4xCO2, however this feature is stronger in CESM1. In CESM2, rapid warming in the tropics (Figs. 6c,g) and southern hemisphere (Figs. 6d,e,h) overwhelms the effect of northern mid to high latitudes in the global mean (Fig 6i). In CESM1, the northern ocean cooling is strong enough to produce the noticeable hiatus or pause in global warming from around year 20 to year 150 seen here (Fig. 6i) and in Figs. 1c,d. Notably, the corresponding regional timeseries in CESM1b-4xCO2 (not shown) and global timeseries (shown in Fig 1d, gray line) are nearly identical to those from CESM1-4xCO2, despite different atmosphere resolution and ocean initialization. This consistency suggests that the NH Land/Ocean behavior shown in Fig 6 is a robust response of CESM1 to 4xCO2 forcing scenarios, not a result of internal variability. The complex response of northern

high-latitudes in the 4xCO2 scenario is of great interest, but will not be explored in this study. The figure also highlights the greater sub-decadal, interannual variability in CESM1, which is particularly evident in the tropics (Figs. 6c,g).

Figure 7 shows scatterplots of decadally-averaged annual-mean $\mathcal{S}_k$ vs T_k in CESM1-4xCO2 and CESM2-4xCO2 for the regions in Fig 5. The figure shows that compact relationships exist between decadally-averaged $\mathcal{S}_k$ and T_k in all regions. Similar results are obtained for longwave radiation (not shown). The figure highlights the regional variations in $\mathcal{S}_k(T)$ as wellas the large absolute differences between shortwave fluxes in CESM1 and CESM2. Regional mean differences of over 10 Wm^{-2} are present, with $\mathcal{S}$ in CESM1 generally lower (stronger shortwave CRE) than in CESM2 in the tropics, and $\mathcal{S}$ in CESM1 higher than in CESM2 in midlatitudes. The behavior of $\mathcal{S}_k$ in Tropical ocean (Fig. 7c) is especially noteworthy showing clearly stronger feedback in CESM2 (consistent with the patterns in Figs. 4c,d), even though absolute values of $\mathcal{S}_k$ are higher, indicating thinner clouds.

4.3.1 Regional linear regression analyses

To quantify the contributions of the regions in Fig. 5a-h to global feedbacks between radiative fluxes and T, we perform linear regressions of $\mathcal{S}_k$ and $\mathcal{L}_k$ vs T_k to determine regional feedback parameters $\lambda_{\mathcal{S};k}$, $\lambda_{\mathcal{L};k}$, as well as regressions of T_k vs $\overline{T}$ to determine and warming amplification factors A_k. These regression parameters are then used in Eq 7. We perform regressions over two periods: years 1–20, to characterize the initial adjustment; and years 100–800, to characterize the long-term slow adjustment. As indicated in Sec. 3.1, model results for years 100-800 are decadally averaged before linear regression is performed. The sub-decadal variability present in the tropics of CESM1 can be expected to affect the regressions for years 1-20. We note this possibility, but will not attempt to address it further in this analysis.

Figure 8 examines the individual components of Eq. 7 for net shortwave and longwave fluxes $\mathcal{S}$ and $\mathcal{L}$, and quantifies how much each analysis region contributes to the total global feedback parameters $\overline{\lambda}_{\mathcal{S}}$ and $\overline{\lambda}_{\mathcal{L}}$. The bars in positions 1-8 of the top panels (Fig. 8a-d) show the complete summands $a_k\lambda_{\mathcal{S};k}A_k$ and $a_k\lambda_{\mathcal{L};k}A_k$ in Eq. 7 for the regions indicated. CESM1-4xCO2 is shown by the black bars, and CESM2-4xCO2 by the red bars. The bars in position 9 show the direct sum over the eight regions, while position 10 shows independent regressions of global means $\overline{\mathcal{S}}$ and $\overline{\mathcal{L}}$ vs $\overline{T}$. The close agreement between the direct sums in position 9 and the independent regression estimates in position 10 validates the regional decomposition in Eq. 7. Numerical values and standard errors for the quantities plotted in Fig. 8 are given in Appendix B.

The nonlinearity in radiation feedbacks can be visually evaluated by comparing the early regression period (years 1–20, Fig. 8a,c) with the later period (years 100–800, Fig. 8b,d). The largest regional contributions to the nonlinearity in shortwave feedback are from Tropical and mid-latitude Southern Oceans (Fig. 8a,b, positions 3 and 4), accounting for almost all of the increase in slope between years 1–20 and 100–800. In contrast, contributions to shortwave feedback from mid and high latitude northern hemisphere and Tropical Land (positions 6 and 7) decrease significantly between years 1–20 and 100–800.

Fig. 8b also shows that the mid-latitude Southern Ocean provides the greatest single contribution to the long-term global shortwave feedback in both CESM1 and CESM2. In CESM2 the mid-latitude Southern Ocean contributes 0.7 $\mathrm{Wm}^{-2}\mathrm{K}^{-1}$ to the global shortwave feedback of about 1.5 $\mathrm{Wm}^{-2}\mathrm{K}^{-1}$, while in CESM1, it contributes around 0.5 $\mathrm{Wm}^{-2}\mathrm{K}^{-1}$ to the total of 1.3 $\mathrm{Wm}^{-2}\mathrm{K}^{-1}$ (Table B4). This is true despite the fact that this region represents only 17% of global surface area. The second largest contributions are from Tropical Ocean, which contributes 0.23 and 0.38 $\mathrm{Wm}^{-2}\mathrm{K}^{-1}$ in CESM1 and CESM2, respectively. The disproportionate contribution of the Southern Ocean to the global shortwave feedback arises from a combination of factors. The intrinsic feedback $\lambda_{\mathcal{S};k}$ for years

100-800 (Fig. 8f) is larger for the mid-latitude Southern Ocean than for any other region analyzed in both CESM1 and CESM2. In addition, the long-term regional warming amplification A_k is over 1.0 in this region for both models (Fig. 8j), significantly larger than for the other two ice-free ocean regions analyzed (N. Atlantic/N. Pacific and Tropical Oceans).

Most importantly for understanding the evolution of climate sensitivity from CESM1 to CESM2, we see in Fig. 8b that the increase in long-term shortwave feedback from CESM1 to CESM2 arises almost entirely from increases in Tropical and mid-latitude Southern oceans, which contribute 0.15 $\mathrm{Wm^{-2}K^{-1}}$ and 0.17 $\mathrm{Wm^{-2}K^{-1}}$, respectively, to the increase in global shortwave feedback from CESM1 to CESM2 (Table B4). A notable decrease in shortwave feedback from CESM1 to CESM2 occurs in the Arctic (-0.14 $\mathrm{Wm^{-2}K^{-1}}$), which is likely related to persistent sea-ice feedback in CESM1. Cloud and surface processes contributing to radiation feedbacks will be examined in Section 4.4.

Regional longwave feedbacks are examined in Figs. 8c,d) and 8g,h. Consistent with Fig. 2 and Table 5, the longwave feedback contributions (Fig. 8c,d) are more similar across CESM1 and CESM2 and also exhibit less change between years 1–20 and 100–800 than shortwave feedbacks. A small increase in longwave feedbacks from CESM1 to CESM2 is present in several regions and globally ($\sim$0.05 $\mathrm{Wm^{-2}K^{-1}}$, Table B6). In both models, the relative contribution of Trop_Ocn to global longwave feedbacks is larger than for shortwave feedbacks.

4.4 Cloud and surface processes

Figure 9 shows the regional breakdown of radiation feedbacks into all-sky, cloudy (CRE) and clear-sky components for CESM1-4xCO2 and CESM2-4xCO2 for Years 100-800 of the experiments. We focus on the slow adjustment because these feedbacks are ultimately responsible for determining the model climate sensitivity. Our initial analysis looks at CESM outputs of total (all-sky) longwave and shortwave TOM radiation and longwave and shortwave cloud radiative forcing, which are then used to diagnose clear-sky fluxes according to Eqs. 2. This gives a first impression of the role of cloud feedbacks. Shortwave cloud feedbacks are then further analyzed using the APRP approach.

In the shortwave (Fig. 9a,d,g) the large increase in feedback between CESM1 and CESM2 arises from the cloudy component (gray bars), with approximately equal contributions from tropical oceans and midlatitude Southern Ocean (Fig. 9g, positions 3 and 4). In CESM1, clear-sky shortwave feedbacks (blue bars) are large in the high-latitude ocean regions (Arctic, position 1, and high-latitude Southern Ocean, position 5), and over Northern Hemisphere land, while in CESM2, clear-sky feedbacks are noticeable only over mid-to-high latitude land regions. Positive high-latitude clear-sky feedbacks over high-latitude oceans produce a global positive clear-sky shortwave feedback in CESM1 that is actually larger than the cloudy feedback. The positive clear-sky feedbacks are accompanied and partially compensated by negative shortwave cloud feedbacks. The net shortwave feedback in these regions nevertheless remains positive in CESM1-4xCO2 as highly reflective snow and ice surfaces disappear and are replaced by somewhat less reflective clouds (e.g.; Frey et al., 2018).

Longwave feedbacks (Figs. 9b,e,h) have changed less in the evolution from CESM1 to CESM2. This is clearly seen by comparing the difference plots for shortwave and longwave feedbacks (Figs. 9g and 9h). Clear-sky longwave feedback is much larger than longwave CRE feedback in both models. Nevertheless, clear-sky and CRE feedback both make comparable contributions to the small differences in longwave feedback between CESM1 and CESM2.

Regional contributions to the net TOM radiation balance are shown in Figs. 9c, f, and i. Figure 9i, in particular, is a useful summary of the net radiation feedback changes

that have occurred between CESM1 and CESM2. Changes to the net radiation feedbacks closely resemble changes in shortwave feedbacks (Fig. 9g). Furthermore, all changes leading to increased climate sensitivity in CESM2 (positive sign in Fig. 9i) arise in CRE feedbacks (gray bars). In high latitude ocean regions, increased CRE feedback in CESM2 is opposed by clear-sky feedback (blue bars). Finally, it is worth noting that the increased tropical ocean shortwave feedback in CESM2 is not compensated by longwave feedbacks (Fig. 9h,i). This is at least in part because increased tropical shortwave CRE feedback in deep convective regions is not compensated by longwave CRE feedback (not shown).

4.4.1 Sea-ice evolution

Figure 10 shows sea-ice concentrations and surface albedo (calculated from model shortwave fluxes at the surface) in the Arctic and high-latitude Southern Oceans in CESM1-4xCO2 and CESM2-4xCO2. Sea-ice concentrations decrease rapidly in CESM2-4xCO2 with little sea-ice remaining in either high-latitude ocean region after year 200. The effective surface albedo in these regions is then essentially constant, explaining the lack of long-term clear-sky shortwave feedback in CESM2-4xCO2. Sea-ice and surface albedo in CESM1-4xCO2 decrease much more slowly, especially in the Arctic, and remain at appreciable levels throughout the 800 years of the experiment. This explains the presence of the large, long-term, clear-sky shortwave feedbacks seen for CESM1 in Fig. 9.

Figures 11a and 11b show regional mean cloud condensates as functions of surface temperature in the Arctic and high-latitude Southern Oceans. As sea-ice decreases in CESM1 (Fig. 10), cloud condensate amounts increase with T throughout the experiment, contributing to the negative shortwave CRE feedback obtained for these regions in CESM1 (Fig. 9a). In CESM2 we see an initial increase in condensate amounts in high-latitude oceans, but during years 100-800 condensate amounts become nearly constant, consistent with the lack of long-term SW CRE feedbacks over high latitude oceans in Fig. 9d.

4.4.2 APRP analysis

We use the APRP approach of Taylor et al. (2007) to further decompose shortwave radiation feedbacks into components related to specific physical processes. Figure 12 compares shortwave CRE feedbacks with respect to $T(x, y)$, i.e. $\lambda_{\mathcal{S}_{cld}}(x, y)$ over years 100-800 with the quantities

$$\Lambda_c(x, y) = -\mathcal{S}^{\downarrow} \frac{\partial \mathcal{A}}{\partial c} \times \lambda_c \tag{11a}$$

$$\Lambda_{\gamma_{cld}}(x, y) = -\mathcal{S}^{\downarrow} \frac{\partial \mathcal{A}}{\partial \gamma_{cld}} \times \lambda_{\gamma_{cld}} \tag{11b}$$

where $\mathcal{A}$, and γ_{cld} are APRP reconstructions of the planetary albedo and cloud scattering (Eq. 8); c is total cloud amount used in the APRP calculation; and $\mathcal{S}^{\downarrow}$ is the incoming solar radiation at TOM. Partial derivatives are evaluated using the analytical expressions for $\mathcal{A}$ in Taylor et al. (2007) (their equations 7, 13, 14, and 15) employing the year 100-800 average values for all parameters in the evaluation. The feedback parameters λ_c and $\lambda_{\gamma_{cld}}$ are determined from linear regressions of c and γ_{cld} vs. $T(x, y)$ over years 100-800.

The quantities Λ_c and $\Lambda_{\gamma_{cld}}$ are the dominant cloud related contributions to the shortwave feedback. Comparing Figs. 12a-b with Figs. 12g-h we see that the sum of Λ_c and $\Lambda_{\gamma_{cld}}$ is very close to the shortwave CRE feedback (and to the all-sky shortwave feedbacks in Figs. 4c-d away from high-latitudes). The individual components represent separate feedbacks associated with cloud scattering properties ($\Lambda_{\gamma_{cld}}$, Figs. 12c-d) and cloud amount (Λ_c Figs. 12e-f). Away from the tropics, these two components of the feedback have comparable magnitudes (1 to 2 $\mathrm{Wm^{-2}K^{-1}}$) in both models. The cloud amount feedback is slightly more positive in CESM2 (Fig. 12f) than in CESM1 (Fig. 12e). In particular, Λ_c over the midlatitude Southern Ocean is similar in CESM1 and CESM2.

Table 6. Global feedback parameters for shortwave flux $\overline{\lambda}_{\mathcal{S}}$, longwave flux $\overline{\lambda}_{\mathcal{L}}$ and net radiative imbalance $\overline{\lambda}_{\mathcal{N}}$ for CESM2-4xCO2 and CESM2-4xCO2-SOM. Note that since $\overline{\mathcal{N}}=\overline{\mathcal{S}}-\overline{\mathcal{L}}$ the fourth column is simply the difference of the second and third columns. Standard errors for the regression slopes are shown in parentheses.

Years	$\overline{\lambda}_{\mathcal{S}}$ ($\mathrm{Wm^{-2}K^{-1}}$)	$\overline{\lambda}_{\mathcal{L}}$ ($\mathrm{Wm^{-2}K^{-1}}$)	$\overline{\lambda}_{\mathcal{N}}$ ($\mathrm{Wm^{-2}K^{-1}}$)
CESM2-4xCO2			
1-20	0.87(0.06)	2.01(0.03)	-1.15 (0.07)
100-800	1.50(0.01)	1.86(0.01)	-0.36 (0.01)
CESM2-4xCO2-SOM			
1-5	0.79(0.10)	2.11(0.04)	-1.32 (0.10)
10-30	1.48(0.03)	1.75(0.02)	-0.28 (0.04)

However, pronounced differences between CESM1 and CESM2 appear in $\Lambda_{\gamma_{cld}}$, the cloud scattering component of the shortwave feedback (Figs. 12c-d). Strong scattering feedbacks $\sim$4 $\mathrm{Wm^{-2}K^{-1}}$ are present in CESM2 in the tropics, which are the main contribution to the stronger overall tropical ocean shortwave feedback noted in Figs.8 and 9 for CESM2. Over the midlatitude Southern Ocean we also see larger values of $\Lambda_{\gamma_{cld}}$ in CESM2 which produce most of the increase in overall shortwave feedback there compared to CESM1.

The main conclusion of Fig. 12 is that cloud scattering feedback explains more of the increased shortwave feedback (and thus increased ECS) in CESM2 than cloud amount feedback. Frey and Kay (2018) found similar increases in scattering feedback and climate sensitivity in CESM1 when they perturbed the model microphysics to increase the amount of supercooled liquid present in clouds. They discuss the possible role of phase feedbacks in suppressing Southern Ocean shortwave feedbacks in the default CESM1, i.e., as ice cloud is replaced by more reflective liquid in a warming climate, cloud albedo increases.

Figure 11c shows average in-cloud liquid and ice phase condensate paths (IWP* and LWP*, Eq. 3) over the mid-latitude Southern Ocean. There is strong long-term decrease of LWP* with T in CESM2 compared to that in CESM1, coupled with a weak increase in IWP*. In CESM1, both LWP* and IWP* decrease with T in the long term, although a clear initial bump in LWP* occurs. For years 100-800, $\lambda_{LWP^*}=-1.67$ $\mathrm{Wm^{-2}K^{-1}}$ in CESM1-4xCO2, more than double $\lambda_{IWP^*}=-0.72$ $\mathrm{Wm^{-2}K^{-1}}$, while in CESM2-4xCO2 $\lambda_{LWP^*}=-4.47$ $\mathrm{Wm^{-2}K^{-1}}$. Without further analysis we cannot quantify how much of the increased SW feedback in CESM2-4xCO2 is due simply to the stronger loss of total condensate with T, and how much is due to the presence of negative phase feedback in CESM1-4xCO2. This analysis is left for a future study.

5 Comparison with slab-ocean experiments and relation to ECS-SOM

Experiments with a thermodynamic slab ocean model (SOM) have been proposed as a way of reducing the computation required to derive estimates of ECS (Danabasoglu & Gent, 2009; Bitz et al., 2012). SOM experiments approach radiative equilibrium within several decades compared to the several hundred years required for ESM simulations with a dynamic ocean. This approach has been used by several investigators to estimate ECS for various versions of CESM (Bitz et al., 2012; Gettelman et al., 2012; Gettelman, Hannay, et al., 2019).

Figure 13 shows $\overline{\mathcal{N}}$ vs. $\Delta\overline{T}$ for CESM1-4xCO2 and CESM2-4xCO2 in SOM and ESM configurations. The sparse density of points for the SOM-4xCO2 runs (gray circles) is a consequence of their rapid equilibration. Nevertheless, there is remarkable over-

lap between $\overline{\mathcal{N}}$ vs. $\Delta\overline{T}$ in the SOM and ESM experiments despite the vastly different time scales with which warming occurs.

The 4xCO2-SOM experiments attain radiative equilibrium $\mathcal{N} \to 0$ and surpass the warming realized in the corresponding ESM runs. Close inspection of the CESM2-4xCO2-SOM results in Fig. 13b shows that for $\Delta\overline{T}$ >11.5K there is an increase in the feedback strength $\overline{\lambda}_{\mathcal{N}}$, leading to a smaller equilibrium warming (∼12.6K) than the equilibrium warming of 13.7K predicted by extrapolating the slow-adjustment behavior of CESM2-4xCO2 (ESM) as discussed in Section 4.1, and suggesting that feedbacks may change in the ESM even after 1000 years (Rugenstein et al., 2019). Fig. 13 also shows results for a 2xCO2 SOM experiment with CESM2 (gray triangles). The scatter of points is large compared to the warming signal, but the overall shape of the $\overline{\mathcal{N}}$ vs $\Delta\overline{T}$ relationship in the 2xCO2 experiment resembles that in the 4xCO2 experiments. Interestingly, values of $\overline{\lambda}_{\mathcal{N}}$ calculated over years 1–100 of the 2xCO2-SOM and 4xCO2-SOM experiments are very similar, -0.42Wm^{-2}K^{-1} and -0.39Wm^{-2}K^{-1} respectively, suggesting that radiation feedbacks in CESM2 are not highly nonlinear with respect to CO_2.

We calculate an "ECS-SOM(4x)" from these 4xCO2 SOM runs as is done in the standard 2xCO2 set-up to determine ECS-SOM, except that we divide the equilibrium warming from the 4xCO2 SOM runs by 2 (Appendix A). Table 1 gives ECS-SOM(4x) values from our experiments compared to values of ECS based on 2xCO2 SOM experiments. Minimal nonlinearity exists in ECS-SOM estimates for CESM1, but moderate nonlinearity is present in CESM2, with ECS-SOM(4x) about 1.15 times higher than ECS-SOM based on 2xCO2 experiments. Plots of $\overline{\mathcal{N}}(\Delta\overline{T})$ in Fig. 13b suggest nonlinearity in initial forcings for CESM2-4xCO2-SOM and CESM2-2xCO2-SOM, with $\mathcal{N}_0 \sim 8$ Wm^{-2} in 4xCO2 compared with ∼3.5 Wm^{-2} in 2xCO2. Assuming similar long-term slopes for $\overline{\mathcal{N}}(\Delta\overline{T})$, these changes in $\overline{\mathcal{N}}_0$ would account for the nonlinearities in ECS-SOM(4x) noted in Table 1.

To identify roughly comparable periods of long-term adjustment in the 4xCO2 SOM and ESM experiments we match $\Delta\overline{T}$ in the SOM to the values obtained in years 100–800 in the corresponding ESM experiments. These points are shown on the plots of $\overline{\mathcal{N}}(\Delta\overline{T})$ (Fig. 13) by larger symbols. For CESM1-4xCO2-SOM we identify years 5-15 as the equivalent long-term adjustment period, while for CESM2-4xCO2-SOM we identify years 10-30. We recognize that this equivalence may miss important regional differences. Figs. 13c,d show sea-ice fraction in the high-latitude Southern and Arctic Oceans as functions of T for years 100–800 in CESM1-4xCO2(ESM) and CESM2-4xCO2(ESM), and the equivalent periods in CESM1-4xCO2-SOM and CESM2-4xCO2-SOM. Sea-ice fractions in the SOM runs are significantly higher than in the ESM at similar values of regional mean T, particularly in the Arctic. Higher Arctic temperatures are reached in CESM2-4xCO2-SOM than in CESM2-4xCO2(ESM) (Fig. 13d). Table 6 shows radiation feedback parameters for CESM2-4xCO2 SOM and ESM experiments.

Figure 14 shows maps of regression coefficients of T versus $\overline{T}$,i.e., $A(x, y)$; $\mathcal{S}$ versus T, i.e., $\lambda_{\mathcal{S}}(x, y)$; and $\mathcal{L}$ versus T, i.e., $\lambda_{\mathcal{L}}(x, y)$ for CESM2-4xCO2-SOM and CESM2-4xCO2 (ESM). The regressions for CESM2-4xCO2 (ESM) are performed over years 100–800 and the corresponding period (years 10–30) in the SOM experiment. The warming amplification factor $A(x, y)$ shows large differences between SOM and ESM experiments. The SOM (Fig. 14a) exhibits a more hemispherically-symmetrical distribution, with both northern and southern high latitudes having broad areas with $A(x, y) > 1.75$. In contrast, the ESM has values of $A(x, y,)$ around 1.25 or below in northern high latitudes, but exceeding 2.5 over much of the Antarctic. Broad areas of the tropics and northern mid-latitudes also warm less in the ESM, while southern mid-latitudes warm more. The role of sea-ice (Figs. 13c,d) in the different pattern of polar amplification in the SOM and ESM is not yet understood.

Radiation flux feedbacks $\lambda_{\mathcal{S}}(x,y)$ and $\lambda_{\mathcal{L}}(x,y)$ shown in Fig. 14c-f are remarkably similar in the SOM and ESM experiments. Feedbacks across the tropical Pacific are somewhat more zonal in the ESM for both shortwave and longwave radiation. This is especially evident in shortwave feedbacks over the tropical eastern Pacific where strong positive feedbacks (>5 $\mathrm{Wm^{-2}K^{-1}}$) appear in the SOM but not in the ESM. This could reflect stronger eastward shifting of tropical Pacific convection in the ESM, consistent with precipitation differences between the SOM and the ESM (not shown). Increasing high-cloud associated with this shift masks the decrease in low-cloud over the eastern Pacific associated with local warming, as reflected in the distribution of Λ_c shown in Fig. 12f.

Overall, the close agreement between the final equilibrium global temperatures under 4xCO2 and in the behavior of $\overline{\mathcal{N}}(\overline{T})$ in SOM and ESM configurations is striking. It is perhaps even more striking that this agreement occurs despite significant regional and hemispheric differences in warming. It is tempting to seek an explanation based on energetic considerations. However, a convincing explanation has not yet been found by the authors. In any event, it appears that CESM's SOM configuration is capable of predicting the total global-mean warming produced in much longer ESM 4xCO2 simulations. It is not clear whether the skillful performance of the CESM SOM is critically dependent on its design, or whether SOM-versions of other Earth-system models behave in a similar way.

6 Comparison with 1%CO2 experiments and relation to TCR

The transient climate response (TCR; Taylor et al., 2012) is determined from fully-coupled ESM experiments in which atmospheric CO_2 concentrations are increased by 1% annually beginning from an equilibrated pre-industrial (piCTL) simulation. The TCR is defined as the average warming in years 61–80 of the 1%CO2 experiment, i.e., when CO_2 concentrations are about 2x the piCTL value (see Appendix A for details of our calculation). Figure 15 shows $\Delta\overline{T}_{1\%}$ (Eq. A1) as a function of time for CESM1 and CESM2 1%CO2 experiments. The two curves are close to each other through year 100, and TCR values determined from these curves are also very close, 2.1K for CESM1 and 2.0K for CESM2 (Table 1). Based on the standard errors for the TCR estimates in Table 1 we conclude that TCR in CESM1 and CESM2 is not significantly different. Nevertheless, we will see that many other aspects of the 1%CO2 experiments for CESM1 and CESM2 exhibit what appear to be large and significant differences.

Figure 15 shows that after year 100, the $\Delta\overline{T}_{1\%}$ values in CESM1-1%CO2 and CESM2-1% begin to diverge. Consistent with its higher sensitivity, CESM2 begins to warm more rapidly. The linear trends over years 100–150 are 0.41(0.02) K $\mathrm{dec^{-1}}$ for CESM1 and 0.52(0.01) K $\mathrm{dec^{-1}}$ for CESM2. Figure 16 shows regional timeseries of ocean surface temperature T_k. These exhibit dramatic differences between CESM1-1%CO2 (gray) and CESM2-1%CO2. (blue). Tropical ocean warming (Fig. 16c) is more pronounced in CESM2 than in CESM1 throughout the 1% experiments, and temperatures in the mid-latitude Southern Ocean (Fig. 16d), while initially lower in CESM2-1%CO2 than in CESM1-1%CO2, also increase more rapidly in CESM2 throughout the 1%CO2 experiments. The behavior of T in these regions is consistent with that seen in the 4xCO2 experiments (red and black curves), that is, in both regions CESM2 warms more rapidly in both 4xCO2 and 1%CO2 scenarios.

There is an interesting reversal of this consistency in northern ocean (Fig. 16a-b) and land (Fig. 16f) regions. In these regions, CESM1-1%CO2 warms more strongly than CESM2-1%CO2, albeit starting from cooler initial conditions. In the North Atlantic/Pacific region (Fig. 16b) CESM1-1%CO2 is briefly almost 1K warmer than CESM2-1%CO2 around year 110. This is a marked contrast with the behavior of the 4xCO2 experiments, in which northern oceans are much warmer, and also warm more rapidly, in CESM2 than in CESM1. These regional differences clearly have implications for the interpretation of abrupt CO_2

increase experiments with respect to 1%CO2 experiments, and will be explored in future studies.

Figure 17 compares regional shortwave fluxes $\mathcal{S}_k$ as functions of T_k in CESM2-1%CO2 (blue) and CESM2-4xCO2 (red). There is surprising overlap in the scatterplots in most regions. However, over the mid-latitude Southern Ocean (Figure 17d) in CESM2-4xCO2, the initial nonlinearity in $\mathcal{S}_k$ discussed in Section 4.3 (e.g. Fig. 8) is clearly evident, but is not evident in CESM2-1%CO2. It is of interest that $\mathcal{S}_k$ for CESM2-1%CO2 and CESM2-4xCO2 over the Southern Ocean appear to converge for $T_k \sim 288$K as CESM2-1%CO2 ends. An extension of the 1%CO2 experiment past year 150, with CO_2 held fixed, would be informative but has not yet been done.

Cloud processes over the Southern Ocean have been shown, here and elsewhere (e.g.; Frey & Kay, 2018), to have important impacts on global shortwave feedbacks and climate sensitivity. Causes for the divergent evolution of $\mathcal{S}_k(T_k)$ over the Southern Ocean in CESM2-4xCO2 and CESM2-1%CO2 have not been identified. The fact that $\mathcal{S}_k(T_k)$ in the two scenarios differs over a common range of T (284–288K) argues against an explanation based on cloud phase. Other possible explanations include differences in boundary layer stability between 4xCO2 and 1%CO2 scenarios. Klein and Hartmann (1993) showed that increased lower tropospheric stability is associated with increased low cloud cover, and Ceppi and Gregory (2017) found relationships between lower tropospheric stability and climate sensitivity in CMIP5 models.

The contrasting behavior of ECS, iECS and TCR in CESM1 and CESM2 is interesting. Clearly, these two versions of CESM do not suggest a linear relationship between TCR and ECS as identified by Flato et al. (2014). The similarity between TCR in CESM1 and CESM2 may be largely spurious, masking large and significant differences in regional warming. The existence of strong North Atlantic cooling in CESM2-1%CO2 compared with CESM1-1%CO2 contrasts sharply with the behavior of 4xCO2 runs and suggests an important difference in ocean heat transport in 1%CO2 versus 4xCO2 scenarios.

This North Atlantic cooling may be responsible for a delayed response of Greenland temperatures and surface mass balance (SMB) in CESM2-1%CO2 experiments. Fig. 18 shows T trends for the North Atlantic and Greenland during 150 years of increasing CO_2. The North Atlantic warms for 40 years, after which temperatures are flat or slightly decreasing until around year 90, and then turn sharply upward. Similarly, Greenland temperatures are flat during years 40–90 before increasing steeply. Sellevold and Vizcaino (2020) have analyzed Greenland Ice Sheet SMB changes, which are driven mainly by increased surface melting associated with warmer temperatures, in a 150-year CESM2-1%CO2 experiment. They found that SMB decreases modestly, by 2.5±0.4 Gt yr^{-2}, during years 1–90, and much more quickly, by 15.9 ± 1.1 Gt yr^{-2}, after year 90. Thus, the Greenland SMB and resulting sea-level contribution in 1%CO2 experiments appear to be closely linked to North Atlantic temperatures and ocean heat transport.

Gregory et al. (2015) examined the role of ocean heat uptake in the 1%CO2 scenario. They found increasing rates of warming in CMIP5 1%CO2 experiments with time which they attribute to declining ocean heat uptake. This leads to the nonlinearity in $\Delta T_{1\%}(t)$ seen in Fig. 15. A convenient measure of this nonlinearity is the ratio $\frac{\langle \Delta T_{1\%} \rangle_{140}}{\mathrm{TCR}}$ where $\langle \Delta T_{1\%} \rangle_{140}$ is the warming around the time of CO_2 quadrupling in the 1%CO2 scenario (year=140). For the CMIP5 ensemble mean this ratio is around 2.4. We derive $\langle \Delta T_{1\%} \rangle_{140}$ of 4.9K for CESM1-1%CO2 and 5.1K for ESM2-1%CO2 (Appendix A) giving ratios of 2.3 and 2.6 respectively. These measures of warming may be better indications of expected conditions at the end of the 21st Century for various realistic scenarios (Gregory et al., 2015), and they appear to better capture differences between CESM1 and CESM2. Nevertheless these measures still mask the profound regional differences in warming evident in Figs. 16 and 18.

7 Summary and Discussion

This study examined abrupt CO_2 and 1%CO_2 increase simulations using two versions of the Community Earth System Model, CESM1 and CESM2. We used results from extended (800+ years) 4xCO2 experiments using fully-coupled, earth system model (ESM) configurations with a dynamic ocean to investigate the origins of CESM2's substantially increased equilibrium climate sensitivity (ECS) compared to CESM1. Table 1 showed several estimates of ECS for CESM1 and CESM2. Values of inferred ECS (iECS) from linear regression of net top-of-model (TOM) radiative imbalance as a function of global mean temperature, $\overline{\mathcal{N}}$ versus $\Delta\overline{T}$, for 4xCO2 experiments (Gregory et al., 2004) depend strongly on the number of years in the regression. In all cases, however, CESM2's iECS is 1K to 2K higher than that of CESM1 (Figure 1b), with values of up to 6.5K for iECS derived from 800 years of CESM2-4xCO2.

Contributions to the increased sensitivity of CESM2 from initial forcing and from radiation feedbacks were examined in Section 4.1. We found an increase in initial forcing $\overline{\mathcal{N}}_0$ in CESM2 of around 1.2 Wm^{-2} compared to CESM1-4xCO2 (Table 4), which appears to originate in rapid initial adjustments of shortwave fluxes and cloud amount (Table 4, Fig. 3). A simple calculation showed that the increased initial forcing contributes as much as half of the increased sensitivity diagnosed from CESM2-4xCO2. However, in CESM2 slab-ocean model experiments using 2xCO2 and 4xCO2 forcing (Section 5) we found that $\overline{\mathcal{N}}_0$ responds nonlinearly to CO_2 increase while radiation feedbacks in CESM2-2xCO2-SOM and CESM2-4xCO2-SOM remain constant. This implies that differences in radiation feedbacks between CESM1 and CESM2 are more central to understanding the increase in equilibrium climate sensitivity (ECS) in CESM2.

Longwave and shortwave contributions to the net radiation feedbacks in CESM1 and CESM2 were separated. We found that global longwave feedbacks in CESM1 and CESM2 are similar, while shortwave feedbacks in the two models are substantially different (Fig 2). Positive shortwave feedback in years 100-800 of the 4xCO2 simulations is significantly higher in CESM2 (1.50 $\mathrm{Wm}^{-2}\mathrm{K}^{-1}$, Table 5) than in CESM1 (1.23, 1.32 $\mathrm{Wm}^{-2}\mathrm{K}^{-1}$). The increased shortwave feedback in CESM2 is responsible for reducing the strength of the net radiation feedback $\overline{\lambda}_{\mathcal{N}}$ (Eq. 10), which in turn increases climate sensitivity. In addition, shortwave feedbacks are responsible for the highly nonlinear behavior of $\overline{\mathcal{N}}(\Delta\overline{T})$ observed in CESM2-4xCO2.

In Sections 4.3 and 4.4, we analyzed regional contributions to the global shortwave feedback using the decomposition in Eq. 7. The largest single contribution to the long-term (years 100–800) shortwave feedback in both models comes from the mid-latitude Southern Ocean between 60°S and 30°S (Fig. 5d), with about half of the global shortwave feedback in both models arising in this region (Fig. 8b), despite the fact that it represents only 17% of the global surface. Increased Southern Ocean shortwave feedback also explains around half of the increase in global shortwave feedback from CESM1 to CESM2, with increased shortwave feedback over Tropical Ocean in CESM2 contributing a comparable amount (Fig. 9g). It is worth emphasizing that the increased tropical shortwave feedback in CESM2 is not compensated by longwave feedbacks and therefore leads to changes in net radiation feedback (Fig. 9h,i).

The Approximate Partial Radiative Perturbation technique (APRP; Taylor et al., 2007) was employed to analyze the contribution of different cloud processes to shortwave feedbacks. APRP showed that the increased feedbacks in CESM2 are related to increased cloud scattering feedback (Fig. 12). We examined the evolution of cloud condensate phase in high and mid-latitudes (Fig. 11). CESM2 is characterized by a much larger proportion of liquid-phase clouds. Over the mid-latitude Southern Ocean we found dramatically enhanced feedback for liquid condensate in CESM2 (-4.5 g m^{-2} K^{-1}) compared to CESM1 (-1.7 g m^{-2} K^{-1}), but stronger feedback for ice condensate in CESM1 than in CESM2 (-0.7 g m^{-2} K^{-1} vs. 0.2 g m^{-2} K^{-1}). Thus, increased scattering feedback over

the Southern Ocean in CESM2 could result from stronger condensate amount feedback, or from reduced negative cloud phase feedback (e.g.; Frey & Kay, 2018). Without further analysis we cannot quantify the role of these two feedback processes. Our results are also consistent with analyses by (Gettelman, Hannay, et al., 2019) who found increased southern ocean radiation feedbacks in CAM6 vs. CAM5 in SST+4K experiments, which they attribute to changes in the treatment of ice-nucleation in the two models.

In Section 5 we compared results from slab-ocean model (SOM) runs with those from the the fully-coupled earth system model (ESM) configurations of CESM1 and CESM2. ECS estimated from slab-ocean model runs (ECS-SOM) has been proposed as a way to reduce the resources required to calculate ECS (e.g.; Danabasoglu & Gent, 2009). ECS-SOM using 2xCO2 forcing has increased from about 4K in CESM1 to 5.4K in CESM2 (Table 1). We found that ECS-SOM(4x) derived from SOM runs subject to 4xCO2 increase agrees remarkably well with iECS derived from long ESM simulations. In addition there is also remarkable similarity in the evolution of $\overline{\mathcal{N}}(\Delta\overline{T})$ between ECS and SOM 4xCO2 experiments (Fig 13). These similarities occur despite the presence of significant regional differences in warming (Fig. 14a,b).

In contrast to ECS the transient climate response (TCR) has not changed between CESM1 and CESM2 (Table 1). TCR is defined as the warming present around year 70 in experiments subject to a 1% annual increase in CO_2, i.e., around the time of CO_2 doubling. In Section 6 we examined the evolution of 1%CO2 CESM1 and CESM2 experiments. While TCR has not changed between CESM1 and CESM2 there are large regional differences in warming between CESM1-1%CO2 and CESM2-1%CO2. Tropical and mid-latitude Southern Oceans warm more rapidly in CESM2-2%CO2 than in CESM1-1%CO2, consistent with the higher ECS of CESM2 (Fig. 16). However, the Arctic and N. Atlantic/N. Pacific in CESM1-1%CO2 and CESM2-1%CO2 behave very differently from what would be expected from their behavior in the 4xCO2 configuration. Northern oceans in CESM2-1%CO2 warm more slowly than in CESM1-1%CO2. The N. Atlantic in CESM2-1%CO2 shows a dramatic multidecadal cooling from years 40 to 80 (Fig. 18a). The origins of this behavior in CESM2-1%CO2 are not yet clear. Similarities in $\mathcal{S}_k(T_k)$ between CESM2-1%CO2 and CESM2-4xCO2 (Fig. 17) argue against an explanation based on cloud feedbacks.

This study explored the evolution of a single modeling system in response to increased CO_2 forcing. We hope this analysis will help in the design of multimodel studies that compare ECS and TCR across the CMIP5 and CMIP6 ensembles. Our study again points to the importance of shortwave cloud radiative effects in determining model climate sensitivity and suggests a key role for ice-phase and mixed-phase microphysics both in high-latitude low clouds and tropical high-clouds. Our study also suggests that model TCR may miss significant regional responses to increasing CO_2, especially in high-latitudes. Both 4xCO2 and 1%CO2 experiments may yield insight into coupled model behavior in more realistic forcing scenarios.

Acknowledgments

The CESM project is supported primarily by the National Science Foundation (NSF). This material is based upon work supported by the National Center for Atmospheric Research, which is a major facility sponsored by the NSF under Cooperative Agreement No. 1852977. Computing and data storage resources, including the Cheyenne supercomputer (doi:10.5065/D6RX99HX), were provided by the Computational and Information Systems Laboratory (CISL) at NCAR.

Appendix A Calculation of ECS and TCR

Calculations of equilibrium climate sensitivity (ECS) and transient climate response (TCR) are subject to uncertainities due both to internal variability in model simulations and to details in calculation procedures, such as the specification of pre-industrial reference temperatures, detrending techniques etc.. Here we describe how the numbers in Table 1 were derived and examine sensitivities to details in the calcuations.

Infrerred ECS (iECS) and TCR are derived from 4xCO2 and 1%CO2 simulations and their respective pre-industrial control (piCTL) simulations. We denote the year in which 4xCO2 and 1%CO2 simulations branch from their piCTL by $Y_{\rm b}$. The duration of the experiments beyond $Y_{\rm b}$ is denoted by $\Delta Y_{\rm exp}$. According to the CMIP protocols (refs) $\Delta Y_{\rm exp}$ is 140 years for the 1%CO2 experiment and 150 years for the 4xCO2 experiment. The piCTLs for CESM1 and CESM2 also run through the period $Y_{\rm b}$ to $Y_{\rm b}$+ 150. Linear fits to the global mean surface temperature $\overline{T}$ from the piCTLs during this period are performed, which we denote by $T_l^*(t)$.

To calculate TCR we first subtract $T_l^*(t)$ from $\overline{T}_{1\%}(t)$, the time series of global mean surface temperature for the corresponding 1%CO2 experiment:

$$\Delta\overline{T}_{1\%}(t) = \overline{T}_{1\%}(t) - T_l^*(t) \tag{A1}$$

TCR is then the average of $\Delta\overline{T}_{1\%}(t)$ over Years 61-80 of the 1%CO2 experiment. This procedure follows that in the ESMValTool (Righi et al., 2020) except that surface temperature is used instead of 2-meter temperature. This approach gives TCR values of 2.1K(0.07K) for CESM1 and 2.0K(0.04K) for CESM2 where the standard errors are shown in parentheses. Standard errors are calculated using bootstrapping with replacement. Bootstrapping is applied to the linear fit T_l^* as well as to the 20-year mean of $\Delta\overline{T}_{1\%}(t)$.

A second average of the warming over years 131-150, $\langle\Delta\overline{T}_{1\%}\rangle_{140}$, is also calculated to characterize the warming attained in the 1%CO2 scenario when CO_2 values have approximately quadrupled, i.e., around year 140 (Gregory et al., 2015). The procedure is identical to that used for the TCR calculate except for the averaging period used. We obtain $\langle\Delta\overline{T}_{1\%}\rangle_{140}$ values of 4.9K(0.08K) for CESM1-1%CO2 and 5.K(0.08K) for CESM2-1%CO2.

To calculate iECS, a linear fit to 150 years of $\overline{\mathcal{N}}(\Delta\overline{T})$ from the 4xCO2 experiment is performed. Here $\Delta\overline{T}$ is defined as the difference of $\overline{T}$ from the 4xCO2 experiment with respect to the average of $\overline{T}$ from the piCTL over Years $Y_{\rm b}$ to $Y_{\rm b}$+150. The linear fit to $\overline{\mathcal{N}}(\Delta\overline{T})$ may be expressed as

$$\overline{\mathcal{N}}_l(\Delta\overline{T}) = \overline{\mathcal{N}}_I + \overline{\lambda}_{\mathcal{N}}\Delta\overline{T} \tag{A2}$$

where $\overline{\lambda}_{\mathcal{N}}$ and $\overline{\mathcal{N}}_I$ are the slope and intercept of the linear fit. Note that elsewhere in the text we use $\overline{\mathcal{N}}_0$ to refer to the intercept for a linear fit to $\overline{\mathcal{N}}(\Delta\overline{T})$ over years 1-20. This particular interval is used to estimate the initial radiative forcing in the 4xCO2 simulations. In the absence of nonlinearity in $\overline{\mathcal{N}}(\Delta\overline{T})$ there would be no significant difference between these quantities.

Equation A2 is inverted for $\overline{\mathcal{N}}_l$=0 to give an equilibrium $\Delta\overline{T}$, which is divided by 2 in 4xCO2 experiments to give the expression for iECS in Equation 10. This approach gives iECS values of 3.4K(0.04K) for CESM1 and 5.3K(0.22K) for CESM2

The calculation of iECS(800) based on 800 years of 4xCO2 differs from the conventional iECS only in how the piCTL $\overline{T}$ reference is defined. Since the piCTL simulations did not extend for 800 years past $Y_{\rm b}$ we use an average of the linear-fit $\overline{T}_{;l}(t)$ extrapolated through year $Y_{\rm b}$+800 to define $\Delta\overline{T}$. Using this method, we derive values of iECS(800) of 4.2K(0.05K) for CESM1 and 6.5K(0.07K) for CESM2.

Again our approach for estimating iECS from 4xCO2 experimental results is close to that outlined by Righi et al. (2020), with the difference that we use T_s instead of T_{2m}. The impact of using T_s rather than T_{2m} is within 0.1K for both TCR and iECS estimates.

The procedure for deriving ECS-SOM estimates from slab-ocean model (SOM) configurations is less well established. We would like to use multiyear averages of $\overline{T}$ from well equilibrated control and 2xCO2 or 4xCO2 SOM experiments to define ECS-SOM. In practice, the choice of averaging periods is somewhat subjective and can lead to small differences in estimates of ECS-SOM. For example, in Figure A1a we show time-series from three SOM experiments using CESM2.0 (1xCO2 in black, 2xCO2 in green, and 4xCO2 in red). Note that all of these experiments are initialized from the same unequilbrated atmospheric state.

Gettelman, Hannay, et al. (2019) used averages over years 40-60 for both the control and 2xCO2 simulations to derive an ECS-SOM of 5.3K for CESM2. If a later period is used for the CESM-2xCO2-SOM (green curve) this estimate will increase since a small additional warming occurs after Year 60. The ECS-SOM of 5.5K for CESM2 in Table 1 is calculated using an average of Years 70-100 for the 2xCO2 experiment and a reference temperature averaged over years 20-75 of CESM2-1xCO2-SOM. We do not advocate either value, but simply present both to illustrate the level of uncertainty that may exist in published numbers for ECS-SOM. ECS-SOM(4x) is calculated using the same reference temperature and an average temperature over years 70-100 of CESM2-4xCO2-SOM. The difference between these values is divided by 2 to account for the 4xCO2 versus 2xCO2 increase.

Another approach to estimating ECS-SOM is to apply the Gregory et al. (2004) approach to $\overline{\mathcal{N}}(\Delta\overline{T})$ from the SOM runs. Results of this approach are shown in Figure A1b. Interestingly the results of this method for CESM2-2xCO2-SOM (green) appear to converge on an ECS-SOM value of around 5.2K, closer to the Gettelman, Hannay, et al. (2019) value, even though this number is based on what appears to be slightly unequlibrated $\overline{T}$ from the 2xCO2 SOM experiment. We note however that the Gregory et al. (2004) method suffers from the same pitfalls when applied to SOM $\overline{\mathcal{N}}(\Delta\overline{T})$ results as it does when applied to full ESM results, i.e., rapid initial adjustment can affect the regression estimate of $\overline{\lambda}_{\mathcal{N}}$. As with full ESM results, better estimates of ECS may be obtained if initial rapid adjustment in $\overline{\mathcal{N}}(\Delta\overline{T})$.

The calculation details discussed in this Appendix have only small impacts on estimates of TCR and ECS, generally less than a few tenths of a degree K. We present them to explain possible discrepancies in published numbers of TCR and ECS for CESM.

Appendix B Tables of regional feedback parameters

This Appendix gives tabulated numbers for slope parameters used in the regional analysis of radiation feedbacks. Tables B1-B6 give numerical values for quantities displayed in Fig 8.

Uncertainties in regression slope parameters are given in the form of standard error estimates shown in (). These are calculated using a bootstrap with replacement approach over the N years in the sample. Where decadal averages have been employed, bootstrapping is performed over $\frac{N}{10}$ decadal means. Where error is given as (0.00) this indicates that the standard error is less than 0.01 in the applicable units.

Table B1. Areal fractions of analysis regions in Fig 5.

Arctic	NAtlPac	Trop. Ocean	SHml Ocn	SHhl Ocn	NH Land	Trop. Land	SH Land
a_k							
2.7%	9.7%	37.6%	17.4%	3.7%	12.4%	12.9%	3.7%

Table B2. Regional warming amplification factors A_k (K K^{-1}) for Years 1-20 and Years 100-800 in CESM1-4xCO2 and CESM2-4xCO2. Standard error estimates are shown in parentheses.

Arctic	NAtlPac	Trop. Ocean	SHml Ocn	SHhl Ocn	NH Land	Trop. Land	SH Land	Global
Years 1-20								
CESM1-4xCO2								
3.57(0.16)	0.97(0.06)	0.76(0.04)	0.81(0.04)	1.45(0.07)	1.37(0.10)	1.02(0.10)	1.05(0.07)	1.00(0.00)
CESM2-4xCO2								
3.26(0.08)	0.98(0.03)	0.78(0.02)	0.67(0.03)	1.21(0.04)	1.51(0.05)	1.05(0.03)	1.15(0.08)	1.00(0.00)
Years 100-800								
CESM1-4xCO2								
2.90(0.08)	0.71(0.01)	0.64(0.01)	1.27(0.02)	2.43(0.03)	1.03(0.02)	0.80(0.01)	1.93(0.02)	1.00(0.00)
CESM2-4xCO2								
1.00(0.04)	0.74(0.01)	0.75(0.00)	1.38(0.01)	1.81(0.01)	0.88(0.01)	1.03(0.00)	1.94(0.02)	1.00(0.00)

Table B3. Regional shortwave radiation feedbacks $\lambda_{\mathcal{S};k}$ (Wm^{-2} K^{-1}, , i.e., linear regression slopes of regional net TOM shortwave radiation $\mathcal{S}_k$ versus regional mean surface temperature $T_{s;k}$ for Years 1-20 and Years 100-800 in CESM1-4xCO2 and CESM2-4xCO2. Standard error estimates are shown in parentheses.

Arctic	NAtlPac	Trop. Ocean	SHml Ocn	SHhl Ocn	NH Land	Trop. Land	SH Land	Global
Years 1-20								
CESM1-4xCO2								
1.12(0.05)	1.67(0.13)	0.41(0.12)	1.16(0.19)	1.49(0.11)	0.80(0.13)	2.07(0.32)	0.41(0.16)	0.99(0.08)
CESM2-4xCO2								
1.14(0.08)	1.15(0.17)	0.54(0.11)	0.82(0.27)	1.39(0.13)	0.99(0.05)	1.13(0.11)	0.42(0.05)	0.87(0.06)
Years 100-800								
CESM1-4xCO2								
2.04(0.03)	1.57(0.05)	0.94(0.04)	2.38(0.03)	1.09(0.02)	0.46(0.03)	1.03(0.06)	0.48(0.02)	1.31(0.01)
CESM2-4xCO2								
0.79(0.05)	1.82(0.03)	1.35(0.02)	2.94(0.02)	0.96(0.02)	0.83(0.02)	0.43(0.02)	0.84(0.01)	1.50(0.01)

Table B4. Complete Regional contributions $a_k A_k \lambda_{\mathcal{S};k}$ (Wm^{-2} K^{-1}) to global shortwave feedback, i.e., summands in Eq 7, for Years 1-20 and Years 100-800 in CESM1-4xCO2 and CESM2-4xCO2. Column 9 shows direct sum of Columns 1–8. Standard error estimates are shown in parentheses.

Arctic	NAtlPac	Trop. Ocean	SHml Ocn	SHhl Ocn	NH Land	Trop. Land	SH Land	$\sum_{k=1}^{8}$
Years 1-20								
CESM1-4xCO2								
0.09(0.01)	0.16(0.02)	0.12(0.04)	0.16(0.03)	0.08(0.01)	0.14(0.03)	0.27(0.07)	0.02(0.01)	1.03(0.10)
CESM2-4xCO2								
0.08(0.01)	0.11(0.02)	0.16(0.04)	0.09(0.04)	0.06(0.01)	0.19(0.02)	0.15(0.02)	0.02(0.00)	0.87(0.06)
Years 100-800								
CESM1-4xCO2								
0.16(0.01)	0.11(0.00)	0.23(0.01)	0.53(0.01)	0.10(0.00)	0.06(0.00)	0.11(0.01)	0.03(0.00)	1.32(0.02)
CESM2-4xCO2								
0.02(0.00)	0.13(0.00)	0.38(0.01)	0.70(0.01)	0.07(0.00)	0.09(0.00)	0.06(0.00)	0.06(0.00)	1.50(0.02)

Table B5. Regional longwave radiation feedbacks $\lambda_{\mathcal{L};k}$ (Wm^{-2} K^{-1}, , i.e., linear regression slopes of regional net TOM longwave radiation $\mathcal{L}_k$ versus regional mean surface temperature $T_{s;k}$ for Years 1-20 and Years 100-800 in CESM1-4xCO2 and CESM2-4xCO2. Standard error estimates are shown in parentheses.

Arctic	NAtlPac	Trop. Ocean	SHml Ocn	SHhl Ocn	NH Land	Trop. Land	SH Land	Global
Years 1-20								
CESM1-4xCO2								
1.05(0.08)	2.11(0.18)	2.38(0.24)	2.25(0.07)	1.18(0.12)	1.75(0.10)	2.65(0.34)	1.65(0.08)	2.05(0.04)
CESM2-4xCO2								
1.18(0.07)	2.20(0.10)	2.12(0.09)	2.70(0.08)	1.09(0.10)	1.53(0.06)	2.65(0.18)	1.59(0.07)	2.01(0.03)
Years 100-800								
CESM1-4xCO2								
1.02(0.03)	2.09(0.03)	2.00(0.04)	2.05(0.02)	1.17(0.01)	1.53(0.02)	2.42(0.05)	1.48(0.01)	1.81(0.01)
CESM2-4xCO2								
1.24(0.04)	2.51(0.02)	1.93(0.02)	2.23(0.01)	1.72(0.02)	1.69(0.01)	1.22(0.01)	1.56(0.00)	1.86(0.01)

Table B6. Complete Regional contributions $a_k A_k \lambda_{\mathcal{L};k}$ (Wm^{-2} K^{-1}) to global longwave feedback, i.e., summands in Eq 7, for Years 1-20 and Years 100-800 in CESM1-4xCO2 and CESM2-4xCO2. Column 9 shows direct sum of Columns 1–8. Standard error estimates are shown in parentheses.

Arctic	NAtlPac	Trop. Ocean	SHml Ocn	SHhl Ocn	NH Land	Trop. Land	SH Land	$\sum_{k=1}^{8}$
Years 1-20								
CESM1-4xCO2								
0.08(0.01)	0.20(0.03)	0.68(0.10)	0.32(0.03)	0.06(0.01)	0.30(0.04)	0.35(0.08)	0.06(0.01)	2.05(0.14)
CESM2-4xCO2								
0.09(0.01)	0.21(0.02)	0.62(0.04)	0.31(0.02)	0.05(0.01)	0.29(0.02)	0.36(0.04)	0.07(0.01)	2.00(0.07)
Years 100-800								
CESM1-4xCO2								
0.08(0.00)	0.14(0.00)	0.48(0.00)	0.45(0.01)	0.10(0.00)	0.20(0.00)	0.25(0.01)	0.11(0.00)	1.81(0.02)
CESM2-4xCO2								
0.03(0.00)	0.18(0.00)	0.54(0.01)	0.53(0.00)	0.12(0.00)	0.19(0.00)	0.16(0.01)	0.11(0.00)	1.86(0.01)

Table B7. Regional warming amplification factors A_k (K K^{-1}) for Years 5-20 in CESM1b-4xCO2-SOM and Years 10-30 in CESM2-4xCO2-SOM. These periods are intended to correspond to Years 100-800 in the corresponding ESM runs. Standard error estimates are shown in parentheses.

Arctic	NAtlPac	Trop. Ocean	SHml Ocn	SHhl Ocn	NH Land	Trop. Land	SH Land	Global
CESM1b-4xCO2-SOM, Years 5-20								
2.37(0.21)	0.95(0.03)	0.70(0.01)	1.12(0.02)	1.83(0.06)	1.19(0.06)	0.89(0.04)	1.54(0.06)	1.00(0.00)
CESM2-4xCO2-SOM, Years 10-30								
1.59(0.06)	0.90(0.02)	0.75(0.01)	1.11(0.02)	1.47(0.03)	1.15(0.04)	1.05(0.02)	1.69(0.05)	1.00(0.00)

Table B8. Regional shortwave and longwave radiation feedbacks $\lambda_{\mathcal{S};k}$ and $\lambda_{\mathcal{L};k}$ (Wm^{-2} K^{-1}) for Years 5-20 in CESM1b-4xCO2-SOM and Years 10-30 in CESM2-4xCO2-SOM. Standard error estimates are shown in parentheses.

Arctic	NAtlPac	Trop. Ocean	SHml Ocn	SHhl Ocn	NH Land	Trop. Land	SH Land	Global
Shortwave radiation feedbacks								
CESM1b-4xCO2-SOM, Years 5-20								
1.75(0.13)	1.61(0.12)	1.02(0.13)	1.97(0.06)	0.80(0.08)	0.78(0.07)	1.16(0.21)	0.28(0.07)	1.22(0.03)
CESM2-4xCO2-SOM, Years 10-30								
1.21(0.10)	1.98(0.11)	1.46(0.09)	2.65(0.08)	1.04(0.06)	0.86(0.05)	0.53(0.08)	0.53(0.04)	1.43(0.04)
Longwave radiation feedbacks								
CESM1b-4xCO2-SOM, Years 5-20								
1.21(0.08)	2.08(0.11)	1.94(0.16)	2.25(0.07)	1.23(0.07)	1.58(0.06)	2.46(0.23)	1.51(0.06)	1.91(0.04)
CESM2-4xCO2-SOM, Years 10-30								
1.08(0.14)	2.09(0.09)	1.57(0.08)	2.38(0.05)	1.62(0.04)	1.49(0.06)	1.25(0.14)	1.49(0.05)	1.70(0.04)

References

Andrews, T., Gregory, J. M., & Webb, M. J. (2015). The dependence of radiative forcing and feedback on evolving patterns of surface temperature change in climate models. *Journal of Climate*, *28*(4), 1630–1648.

Andrews, T., Gregory, J. M., Webb, M. J., & Taylor, K. E. (2012). Forcing, feedbacks and climate sensitivity in cmip5 coupled atmosphere-ocean climate models. *Geophysical Research Letters*, *39*(9).

Armour, K. C., Bitz, C. M., & Roe, G. H. (2013). Time-Varying Climate Sensitivity from Regional Feedbacks. *J. Climate*, *26*, 4518–4534. doi: 10.1175/JCLI-D-12-00544.1

Bitz, C. M., Shell, K. M., Gent, P. R., Bailey, D. A., Danabasoglu, G., Armour, K. C., ... Kiehl, J. T. (2012). Climate sensitivity of the community climate system model, version 4. *Journal of Climate*, *25*(9), 3053-3070. doi: 10.1175/JCLI-D-11-00290.1

Bogenschutz, P. A., Gettelman, A., Morrison, H., Larson, V. E., Craig, C., & Schanen, D. P. (2013). Higher-order turbulence closure and its impact on climate simulations in the community atmosphere model. *Journal of Climate*, *26*(23), 9655–9676.

Ceppi, P., & Gregory, J. M. (2017). Relationship of tropospheric stability to climate sensitivity and earth's observed radiation budget. *Proceedings of the National Academy of Sciences*, *114*(50), 13126–13131. doi: 10.1073/pnas.1714308114

Charney, J. G., Arakawa, A., Baker, D. J., Bolin, B., Dickinson, R. E., Goody, R. M., ... Wunsch, C. I. (1979). *Carbon dioxide and climate: a scientific assessment*. National Academy of Sciences, Washington, DC.

Danabasoglu, G., & Gent, P. R. (2009). Equilibrium climate sensitivity: Is it accurate to use a slab ocean model? *Journal of Climate*, *22*(9), 2494–2499.

Danabasoglu, G., Lamarque, J.-F., Bacmeister, J., Bailey, D., DuVivier, A., Edwards, J., ... others (2020). The community earth system model version 2 (CESM2). *Journal of Advances in Modeling Earth Systems*, *12*(2), e2019MS001916.

Etminan, M., Myhre, G., Highwood, E., & Shine, K. (2016). Radiative forcing of carbon dioxide, methane, and nitrous oxide: A significant revision of the methane radiative forcing. *Geophysical Research Letters*, *43*(24), 12–614.

Eyring, V., Bony, S., Meehl, G. A., Senior, C. A., Stevens, B., Stouffer, R. J., & Taylor, K. E. (2016). Overview of the coupled model intercomparison project phase 6 (CMIP6) experimental design and organization. *Geoscientific Model Development (Online)*, *9*(LLNL-JRNL-736881).

Flato, G., Marotzke, J., Abiodun, B., Braconnot, P., Chou, S. C., Collins, W., ... others (2014). Evaluation of climate models. In *Climate change 2013: the physical science basis. contribution of working group i to the fifth assessment report of the intergovernmental panel on climate change* (pp. 741–866). Cambridge University Press.

Frey, W. R., & Kay, J. E. (2018). The influence of extratropical cloud phase and amount feedbacks on climate sensitivity. *Climate dynamics*, *50*(7-8), 3097–3116.

Frey, W. R., Morrison, Kay, J., Guzman, R., & Chepfer, H. (2018). The combined influence of observed southern ocean clouds and sea ice on top-of-atmosphere albedo. *Journal of Geophysical Research: Atmospheres*, *123*(9), 4461–4475.

Gettelman, A., Hannay, C., Bacmeister, J., Neale, R., Pendergrass, A., Danabasoglu, G., ... others (2019). High climate sensitivity in the community earth system model version 2 (CESM2). *Geophysical Research Letters*, *46*(14), 8329–8337.

Gettelman, A., Kay, J., & Shell, K. (2012). The evolution of climate sensitivity and climate feedbacks in the community atmosphere model. *Journal of Climate*, *25*(5), 1453–1469.

Gettelman, A., Mills, M., Kinnison, D., Garcia, R., Smith, A., Marsh, D., ... others (2019). The whole atmosphere community climate model version 6 (waccm6). *Journal of Geophysical Research: Atmospheres*, *124*(23), 12380–12403.

Gettelman, A., Morrison, H., Santos, S., Bogenschutz, P., & Caldwell, P. (2015). Advanced two-moment bulk microphysics for global models. part ii: Global model solutions and aerosol–cloud interactions. *Journal of Climate*, *28*(3), 1288–1307.

Gregory, J., Andrews, T., & Good, P. (2015). The inconstancy of the transient climate response parameter under increasing co2. *Philosophical Transactions of the Royal Society A: Mathematical, Physical and Engineering Sciences*, *373*(2054), 20140417.

Gregory, J., Ingram, W., Palmer, M., Jones, G., Stott, P., Thorpe, R., ... Williams, K. (2004). A new method for diagnosing radiative forcing and climate sensitivity. *Geophysical Research Letters*, *31*(3).

Held, I. M., Winton, M., Takahashi, K., Delworth, T., Zeng, F., & Vallis, G. K. (2010). Probing the fast and slow components of global warming by returning abruptly to preindustrial forcing. *Journal of Climate*, *23*(9), 2418–2427.

Hoesly, R. M., Smith, S. J., Feng, L., Klimont, Z., Janssens-Maenhout, G., Pitkanen, T., ... others (2018). Historical (1750–2014) anthropogenic emissions of reactive gases and aerosols from the community emissions data system (ceds). *Geoscientific Model Development (Online)*, *11*(PNNL-SA-123932).

Hurrell, J. W., Holland, M. M., Gent, P. R., Ghan, S., Kay, J. E., Kushner, P. J.,

... others (2013). The community earth system model: a framework for collaborative research. *Bulletin of the American Meteorological Society*, *94*(9), 1339–1360.

Iacono, M. J., Delamere, J. S., Mlawer, E. J., Shephard, M. W., Clough, S. A., & Collins, W. D. (2008). Radiative forcing by long-lived greenhouse gases: Calculations with the aer radiative transfer models. *Journal of Geophysical Research: Atmospheres*, *113*(D13).

Kay, J. E., Deser, C., Phillips, A., Mai, A., Hannay, C., Strand, G., ... others (2015). The community earth system model (CESM) large ensemble project: A community resource for studying climate change in the presence of internal climate variability. *Bulletin of the American Meteorological Society*, *96*(8), 1333–1349.

Kay, J. E., Medeiros, B., Hwang, Y.-T., Gettelman, A., Perket, J., & Flanner, M. (2014). Processes controlling southern ocean shortwave climate feedbacks in cesm. *Geophysical Research Letters*, *41*(2), 616–622.

Klein, S. A., & Hartmann, D. L. (1993). The seasonal cycle of low stratiform clouds. *Journal of Climate*, *6*(8), 1587–1606.

Li, C., von Storch, J.-S., & Marotzke, J. (2013). Deep-ocean heat uptake and equilibrium climate response. *Climate Dynamics*, *40*(5-6), 1071–1086.

Lipscomb, W. H., Price, S. F., Hoffman, M. J., Leguy, G. R., Bennett, A. R., Bradley, S. L., ... others (2019). Description and evaluation of the community ice sheet model (cism) v2. 1. *Geoscientific Model Development*, *12*(1), 387–424.

Morrison, H., & Gettelman, A. (2008). A new two-moment bulk stratiform cloud microphysics scheme in the community atmosphere model, version 3 (cam3). part i: Description and numerical tests. *Journal of Climate*, *21*(15), 3642–3659.

Neale, R., Bacmeister, J., & Hannay, C. (2020). Description of cam6. *Journal of Advances in Modeling Earth Systems*.

Otto-Bliesner, B. L., Brady, E. C., Fasullo, J., Jahn, A., Landrum, L., Stevenson, S., ... Strand, G. (2016). Climate variability and change since 850 ce: An ensemble approach with the community earth system model. *Bulletin of the American Meteorological Society*, *97*(5), 735-754. doi: 10.1175/BAMS-D-14-00233.1

Righi, M., Andela, B., Eyring, V., Lauer, A., Predoi, V., Schlund, M., ... Zimmermann, K. (2020). Earth system model evaluation tool (esmvaltool) v2.0 – technical overview. *Geoscientific Model Development*, *13*(3), 1179–1199. Retrieved from `https://www.geosci-model-dev.net/13/1179/2020/` doi: 10.5194/gmd-13-1179-2020

Rugenstein, M., Bloch-Johnson, J., Abe-Ouchi, A., Andrews, T., Beyerle, U., Cao, L., ... others (2019). Longrunmip–motivation and design for a large collection of millennial-length ao-gcm simulations. *Bulletin of the American Meteorological Society*, *100*(2019), 2551–2570. doi: https://doi.org/10.1175/BAMS-D-19-0068.1

Sellevold, R., & Vizcaino, M. (2020). Global warming threshold and mechanisms for accelerated greenland ice sheet surface mass loss. *J. Adv. Model. Earth Syst.*. (In review)

Senior, C. A., & Mitchell, J. F. (2000). The time-dependence of climate sensitivity. *Geophysical Research Letters*, *27*(17), 2685–2688.

Stevenson, S., Otto-Bliesner, B., Fasullo, J., & Brady, E. (2016). "el niño like" hydroclimate responses to last millennium volcanic eruptions. *Journal of Climate*, *29*(8), 2907–2921.

Stouffer, R. J., & Manabe, S. (1999). Response of a coupled ocean–atmosphere model to increasing atmospheric carbon dioxide: Sensitivity to the rate of increase. *Journal of Climate*, *12*(8), 2224–2237.

Taylor, K. E., Crucifix, M., Braconnot, P., Hewitt, C., Doutriaux, C., Broccoli, A., ... Webb, M. (2007). Estimating shortwave radiative forcing and response in

climate models. *Journal of Climate*, *20*(11), 2530–2543.

Taylor, K. E., Stouffer, R. J., & Meehl, G. A. (2012). An overview of CMIP5 and the experiment design. *Bulletin of the American Meteorological Society*, *93*(4), 485–498.

Williams, K., Ingram, W., & Gregory, J. (2008). Time variation of effective climate sensitivity in gcms. *Journal of Climate*, *21*(19), 5076–5090.

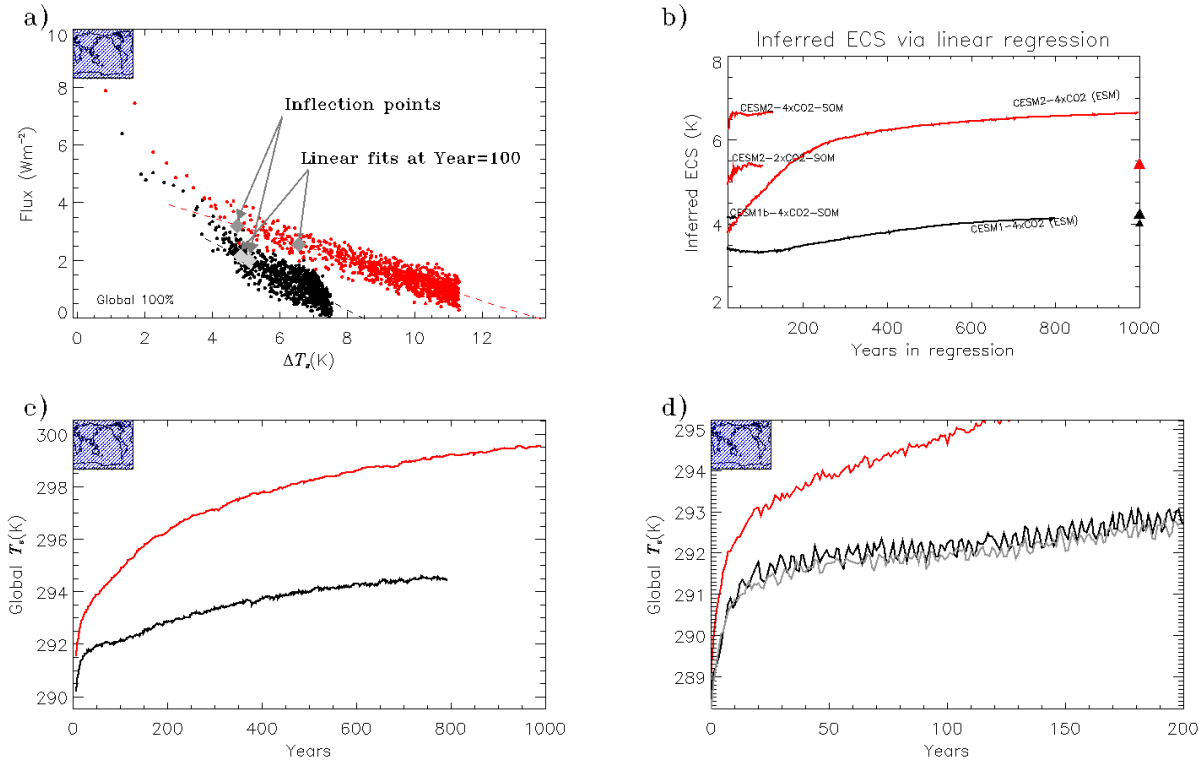

Figure 1. **a)** Annual-mean, global top-of-model radiation imbalance $\overline{\mathcal{N}}$ as a function of annual-mean, global-mean surface temperature change $\Delta\overline{T}$ for abrupt 4xCO2 experiments CESM1-4xCO2 (black) and CESM2-4xCO2 (red). Dashed lines show linear fits to $\overline{\mathcal{N}}(\Delta\overline{T})$ for years 100–800. Two points are indicated on each $\overline{\mathcal{N}}(\Delta\overline{T})$ relationship: Values of linear fits at year 100 and diagnosed inflection points (see Section 3.3). **b)** Inferred equilibrium climate sensitivities (iECS) from linear regressions: Horizontal axis gives number of years used in the regression. Long curves extending to 800 years and beyond show iECS derived for CESM1-4xCO2 (black) and CESM2-4xCO2 (red) from linear regressions of $\overline{\mathcal{N}}(\Delta\overline{T})$. Shorter red curves shows iECS derived from a 2xCO2-SOM experiment with CESM2 (CESM2-2xCO2-SOM, Table 3) and from a 4xCO2 SOM experiment with CESM2 (CESM2-4xCO2-SOM). Short black indicates iECS derived from CESM1b-4xCO2-SOM. Black and red triangles on right vertical axis show values of ECS-SOM for CESM1 (4.0K, 4.2K) and CESM2 (5.5K). **c)** Global mean surface temperature $\overline{T}$ as a function of time for CESM1-4xCO2 (black) and CESM2-4xCO2 (red). **d)** As **c** except focusing on first 200 years of experiments. Gray line shows results for CESM1b-4xCO2.

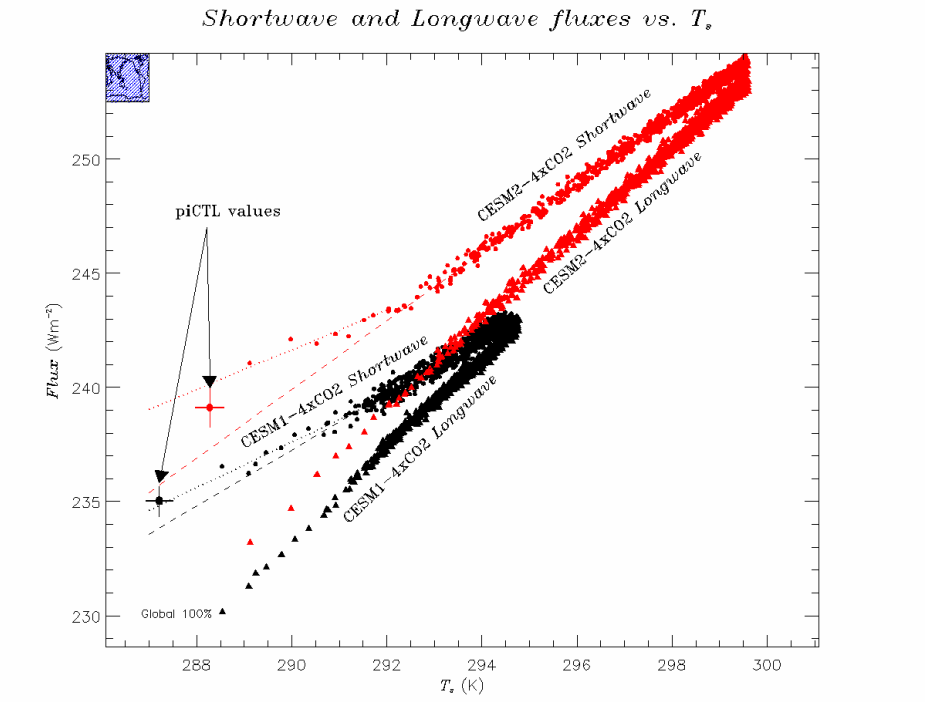

Figure 2. Annual-mean, global top-of-atmosphere net shortwave $\overline{\mathcal{S}}$ and longwave $\overline{\mathcal{L}}$ radiative fluxes as functions of annual-mean, global-mean surface temperature $\overline{T}$ for CESM1 (black) and CESM2 (red). Filled circles show annual mean $\overline{\mathcal{S}}$ for 4xCO2 experiments, and filled triangles show $\overline{\mathcal{L}}$. Large circles with error bars (2σ) show equilibrated multiyear means of $\overline{\mathcal{S}}$ and $\overline{\mathcal{L}}$ as functions of $\overline{T}$ from the corresponding pre-industrial control runs (piCTLs) for each model. Note that in the piCTLs, multiyear means of $\overline{\mathcal{S}}$ and $\overline{\mathcal{L}}$ are within 0.1 Wm^{-2} of each other. Long dashes show extrapolations of linear regression fits to $\overline{\mathcal{S}}$ for years 100–800 for CESM1-4xCO2 extrapolation (black dashed line) and CESM2-4xCO2 (red dashed line). Dotted lines show linear fits for years 1–20. Slopes $\overline{\lambda}_{\mathcal{S}}$ of these lines are given in Table 5.

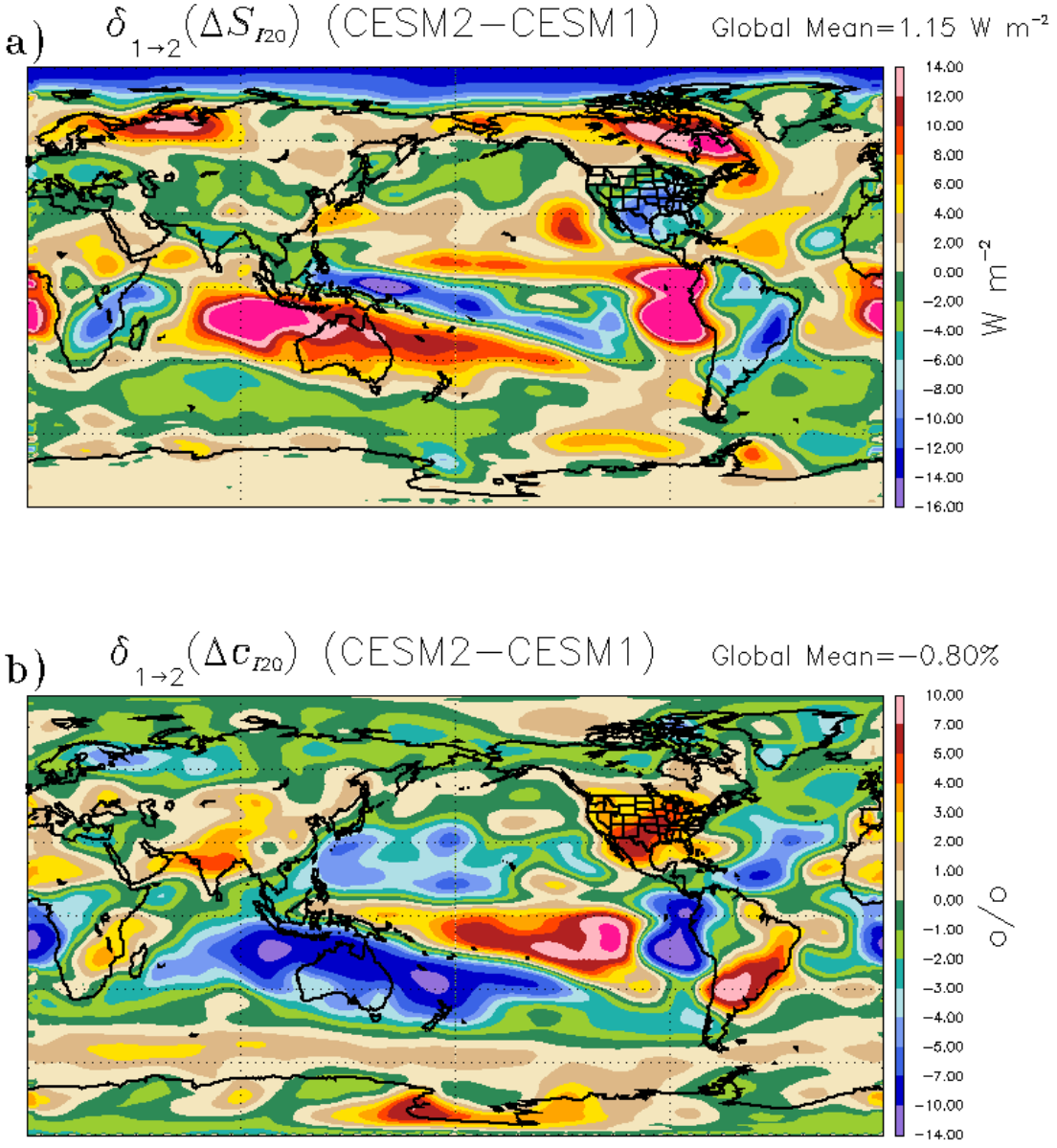

Figure 3. **a)** Difference in initial shortwave adjustment associated with CO_2 quadrupling between CESM1 and CESM2 as a function of latitude and longitude. **b)** Difference in cloud amount adjustment. In both panels positive numbers indicate stronger adjustment in CESM2.

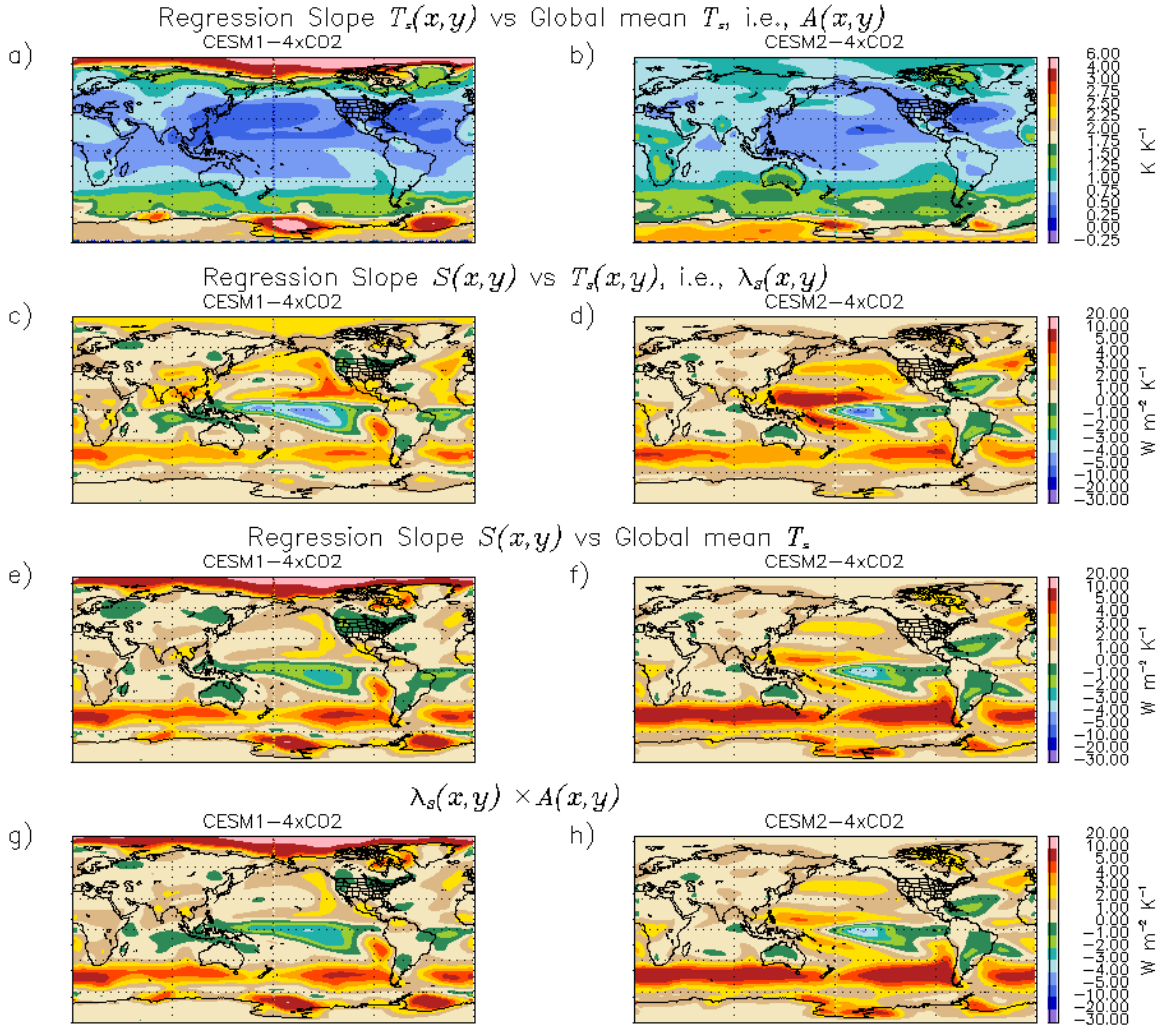

Figure 4. Slopes from linear regressions over years 100–800 of CESM1-4xCO2 (**a, c, e, g**) and CESM2-4xCO2 (**b, d, f, h**) as functions of latitude and longitude: **a, b)** $A(x, y)$ - local warming amplification factor from regression of local temperature versus global mean temperature $\overline{T}$; **c, d)** $\lambda_{\mathcal{S}}(x, y)$ - local shortwave feedback from regression of shortwave radiation $\mathcal{S}$ versus temperature; **e, f)** Slope of local shortwave flux versus global mean temperature $\overline{T}$; **g, h)** Product of $A(x, y)$ and $\lambda_{\mathcal{S}}(x, y)$.

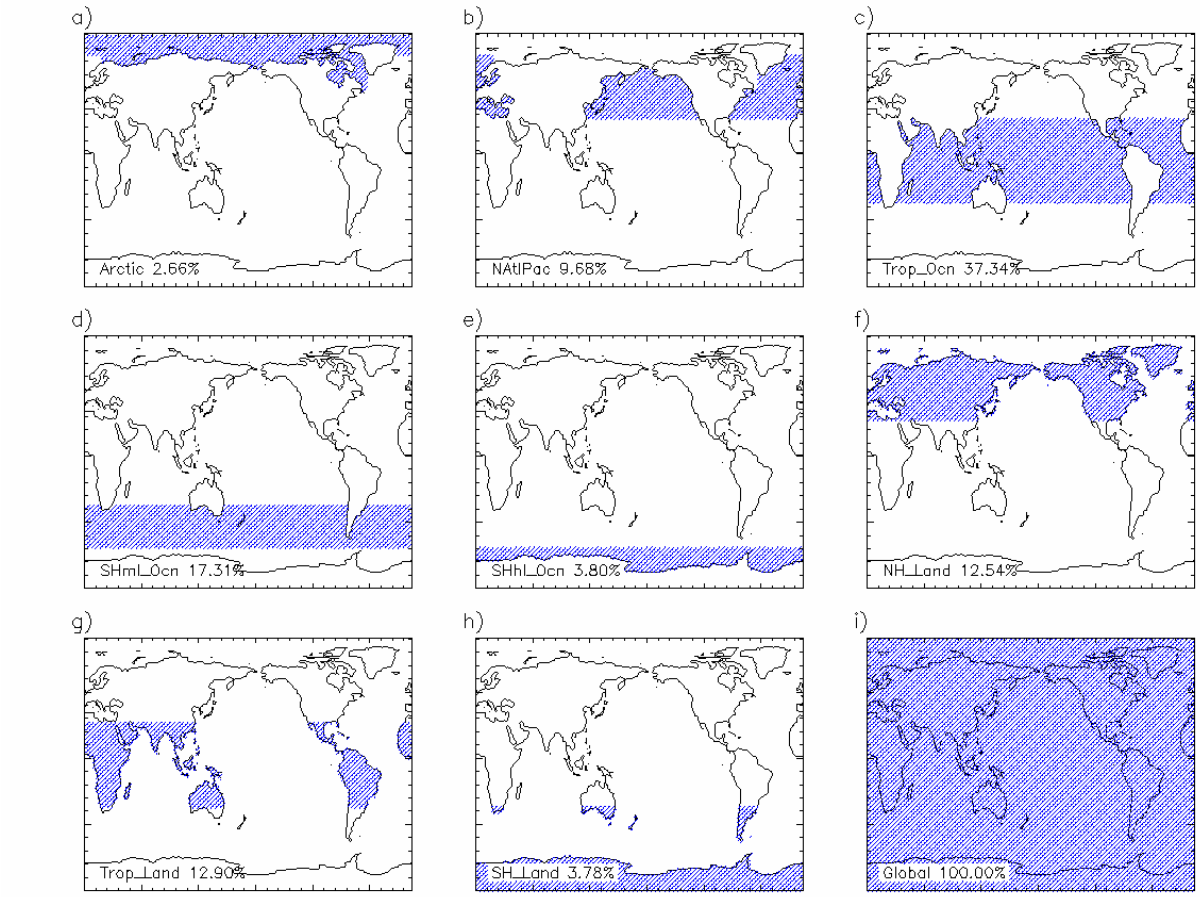

Figure 5. Regions used for feedback analyses: **a)** Arctic Ocean; **b)** N. Atlantic and N. Pacific north of 30°N (NAtlPac); **c)** Ocean between 30°S and 30°N (Trop_Ocn); **d)** Mid-latitude Southern Ocean between 30°S and 60°S (SHml_Ocn); **e)** High-latitude Southern Ocean south of 60°S (SHhl_Ocn); **f)** Land north of 30°N (NH_Land); **g)** Land between 30°S and 30°N (Trop_Land); **h)** Land south of 30°S (SH_Land); and **i)** Global. Approximate fractional area of regions are given in each panel.

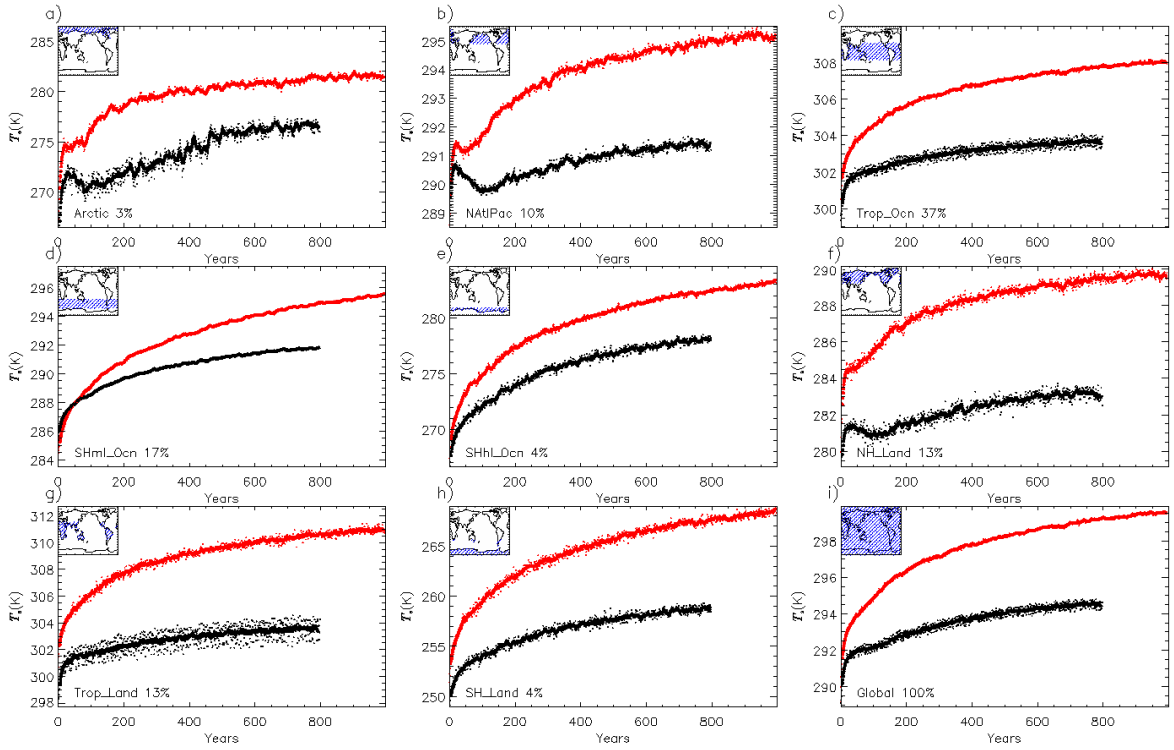

Figure 6. Regional-mean timeseries of surface temperature T for regions in Fig 5. Black shows CESM1-4xCO2 and red shows CESM2-4xCO2. Solid lines show annual means subjected to a running 10-year mean. Symbols show annual means.

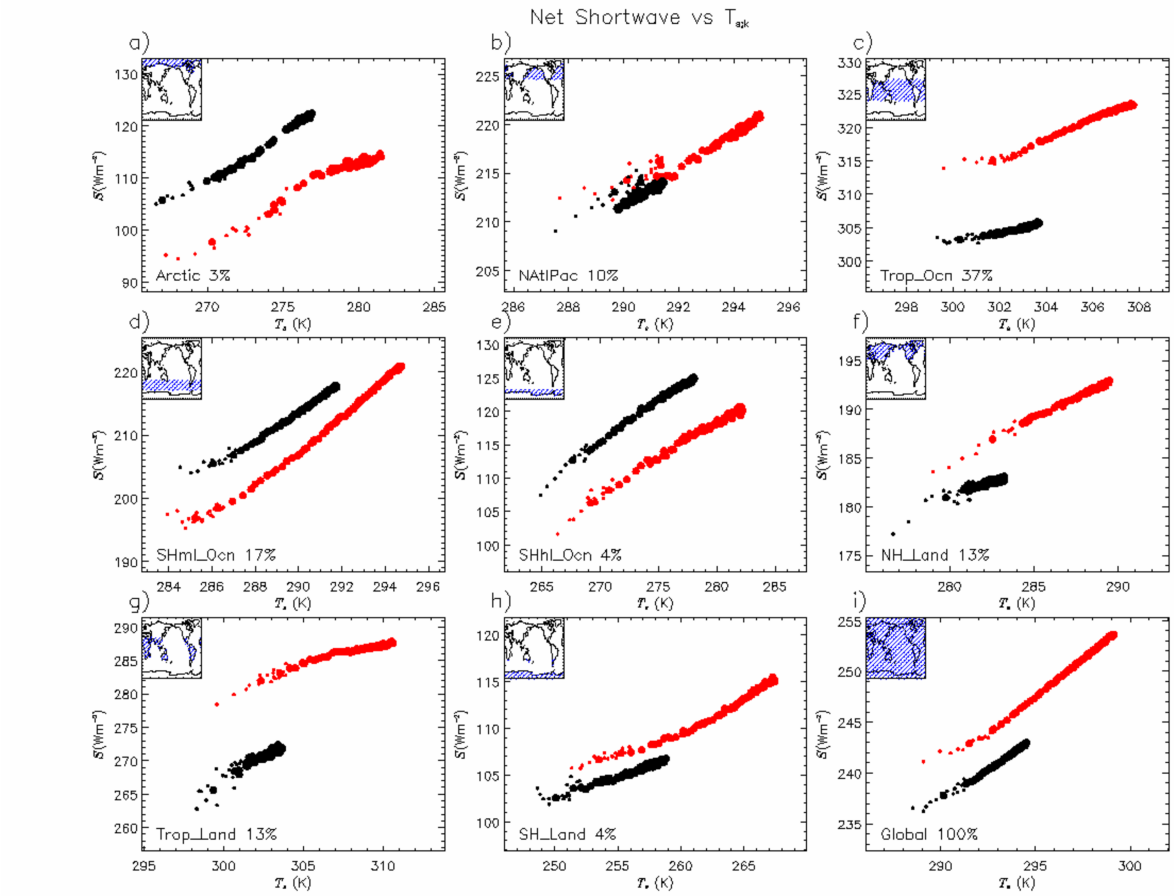

Figure 7. Regional mean, net shortwave radiation $\mathcal{S}_k$ as a function of mean surface temperature T_k in CESM1-4xCO2 (black circles) and CESM2-4xCO2 (red circles) for regions in Fig 5. Larger circles show decadal averages for entire 4xCO2 simulations. Smaller circles show annual means for years 1-20.

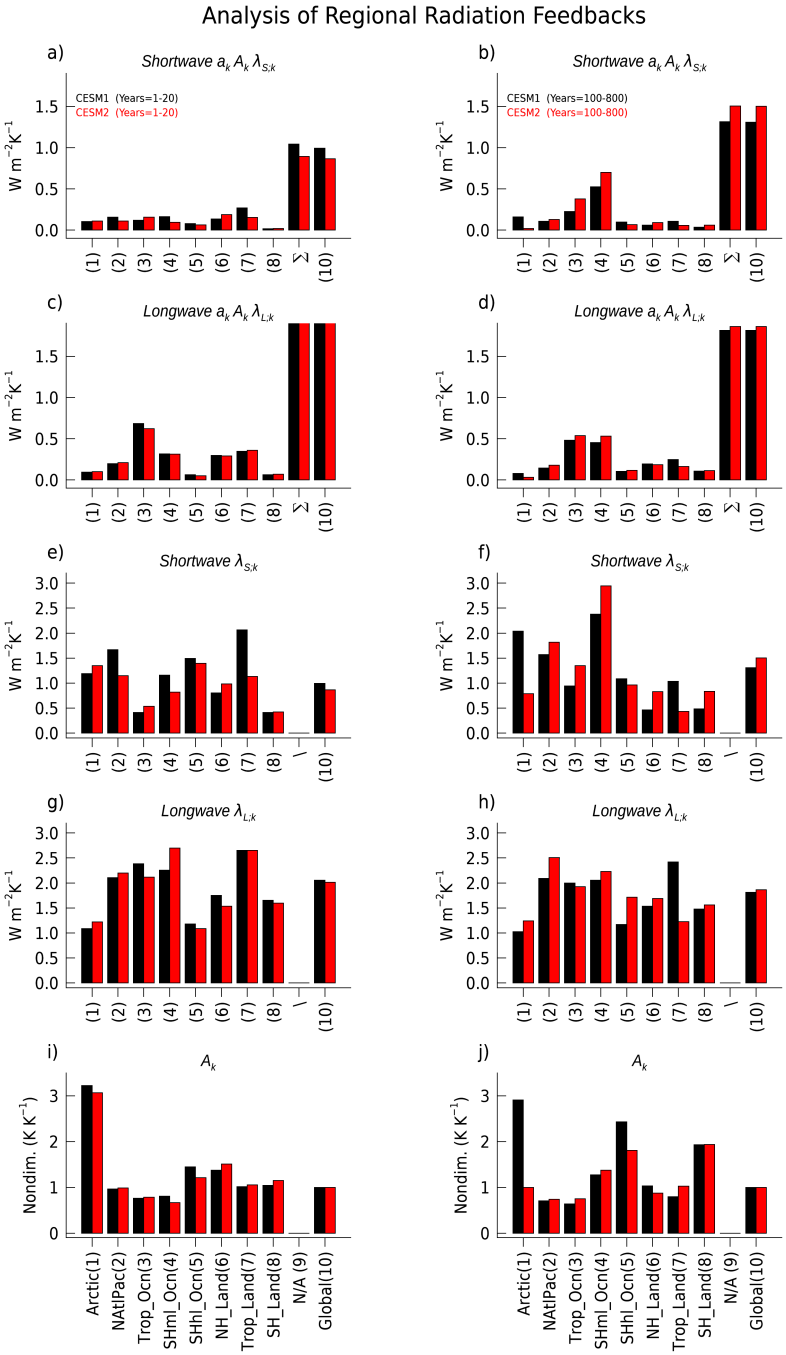

Figure 8. Regional contributions to global shortwave and longwave feedback parameters $\overline{\lambda}_{\mathcal{S}}$ and $\overline{\lambda}_{\mathcal{L}}$ computed using Eq. 7. Left panels (**a, c, e, g, i**) show results for the early phase of the 4xCO2 runs (years 1–20), and right panels (**d, b, f, h, j**) show results for the later "slow adjustment" phase (years 100–800). **a**, **b)** Complete regional shortwave contributions $a_k A_k \lambda_{\mathcal{S};k}$. **c**, **d)** Complete regional longwave contributions $a_k A_k \lambda_{\mathcal{L};k}$. **e**, **f)** Linear regression slopes $\lambda_{\mathcal{S};k}$ of shortwave radiation $\mathcal{S}_k$ versus T_k in each region. **g**, **h)** Linear regression slopes $\lambda_{\mathcal{L};k}$ for longwave radiation. **i**, **j)** Linear regression slopes A_k of regional mean temperatures T_k versus $\overline{T}$. Black bars indicate CESM1-4xCO2 and red bars indicate CESM2-4xCO2. Each panel shows 10 pairs of bars. Positions 1-8 show quantities for the regions shown in Fig. 5. In **a-d**, the bars in position 9 show direct sums over the 8 terms shown to the left, while position 10 shows independent regressions of $\overline{\mathcal{S}}$ and $\overline{\mathcal{L}}$ versus $\overline{T}$.

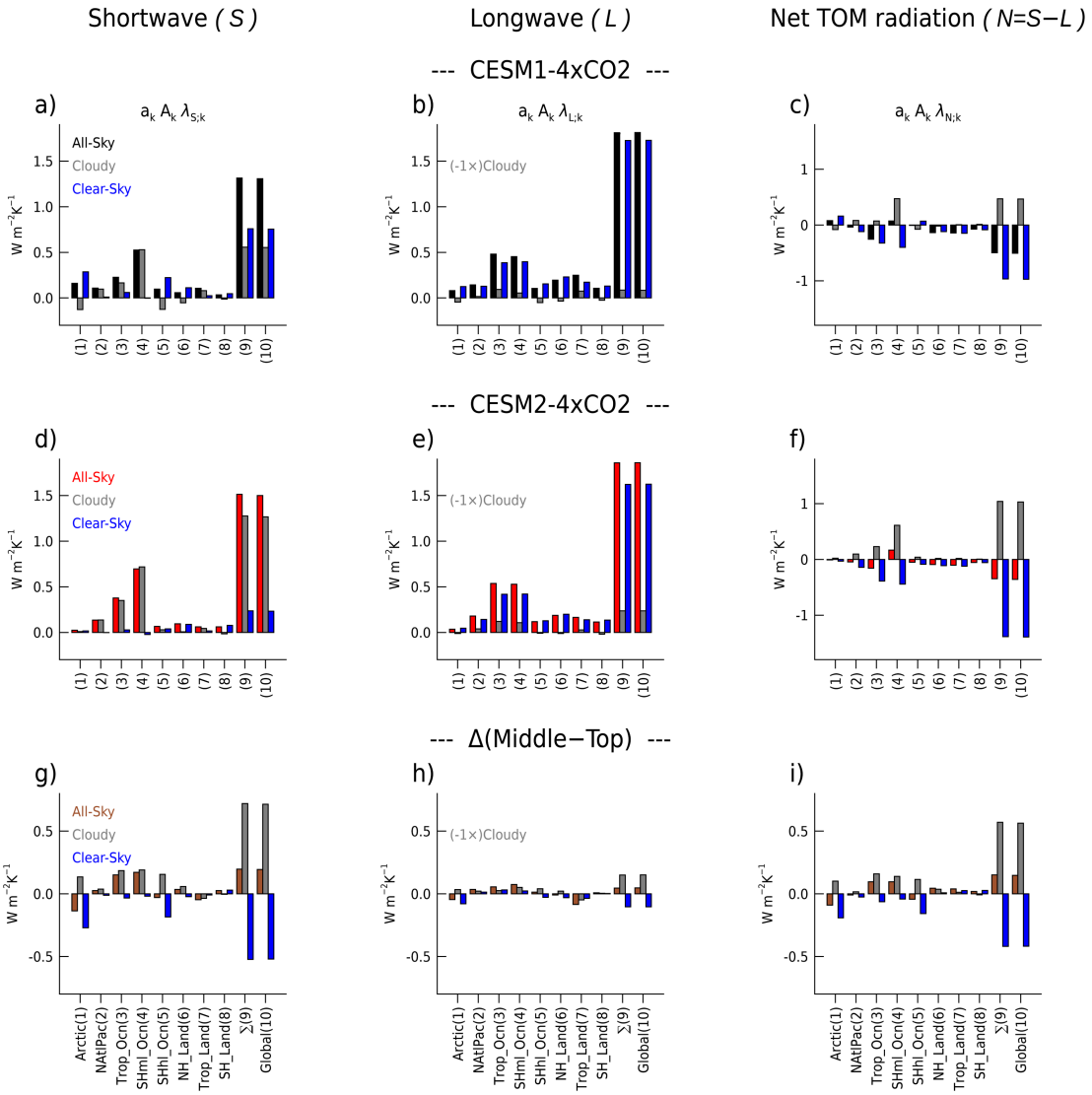

Figure 9. Decomposition of radiation feedbacks for years 100-800 in CESM1-4xCO2 (**a-c**), CESM2-4xCO2 (**d-f**), and differences (**g-i**) into all-sky (black, red and brown bars), cloud radiative effect (CRE, gray bars) and clear-sky (blue bars) components by region as in Fig. 8. First column **(a,d,g)** shows total regional contributions to global shortwave feedbacks. Second column **(b,e,h)** shows total regional contributions to global longwave feedbacks. The longwave CRE contribution has been multiplied by −1 so that bars for clear-sky and CRE feedbacks are additive in the same sense as in the shortwave. Third column **(c,f,i)** shows contributions to net TOM radiation feedbacks. More negative values of net TOM radiation feedback correspond to reduced climate sensitivity. Thus, positive brown bars in in panel **i** indicate a regional contribution to increased climate sensitivity in CESM2.

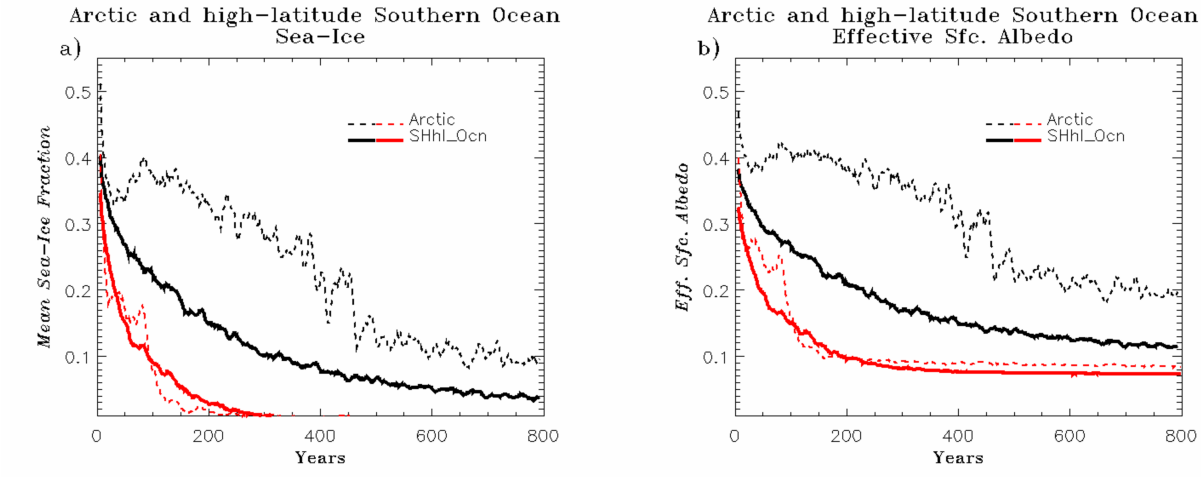

Figure 10. **a)** Annual mean sea-ice fraction as a function of time for Arctic and high-latitude Southern Oceans in CESM1-4xCO2 (black) and CESM2-4xCO2 (red). **b)** As in **a** except for surface albedos as functions of time. Dashed lines show fraction and surface albedo in the Arctic Ocean (Fig. 5a), and solid lines show fraction and surface albedo in the high-latitude Southern Ocean (Fig. 5e).

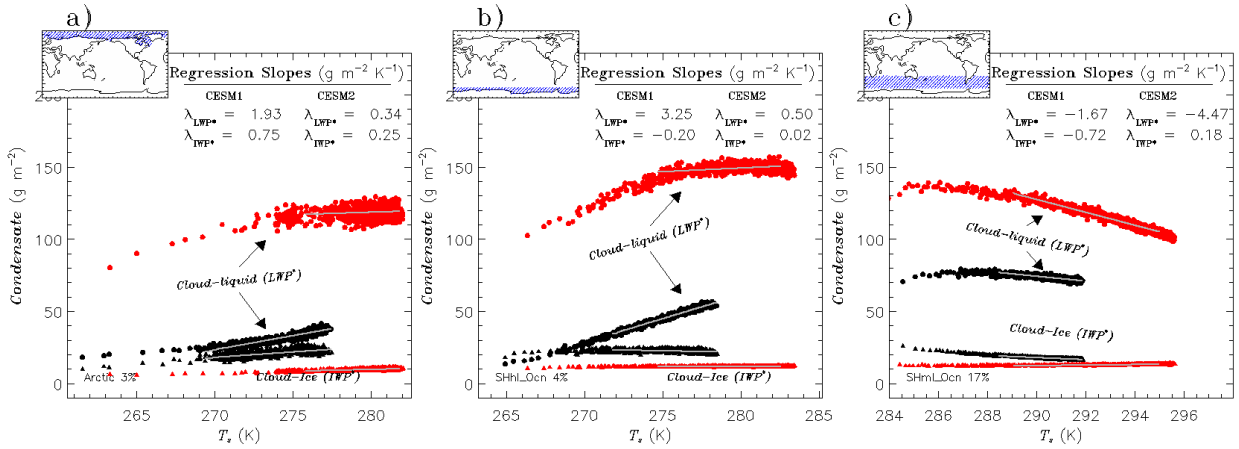

Figure 11. Regional-mean, in-cloud condensate paths (IWP* and LWP*, Eq. 3) in g m^{-2} as functions of regional mean T_k in CESM1-4xCO2 (black) and CESM2-4xCO2 (red): **a)** Arctic Ocean; **b)** High-latitude Southern Ocean; and **c)** Mid-latitude Southern Ocean. Circles show cloud liquid water path LWP*. Triangles show cloud-ice water path IWP*. Gray lines show linear fits over years 100-800. Regression slopes $\lambda_{LWP^*;k}$ and $\lambda_{IWP^*;k}$ for these fits are given in upper right corner of each panel.

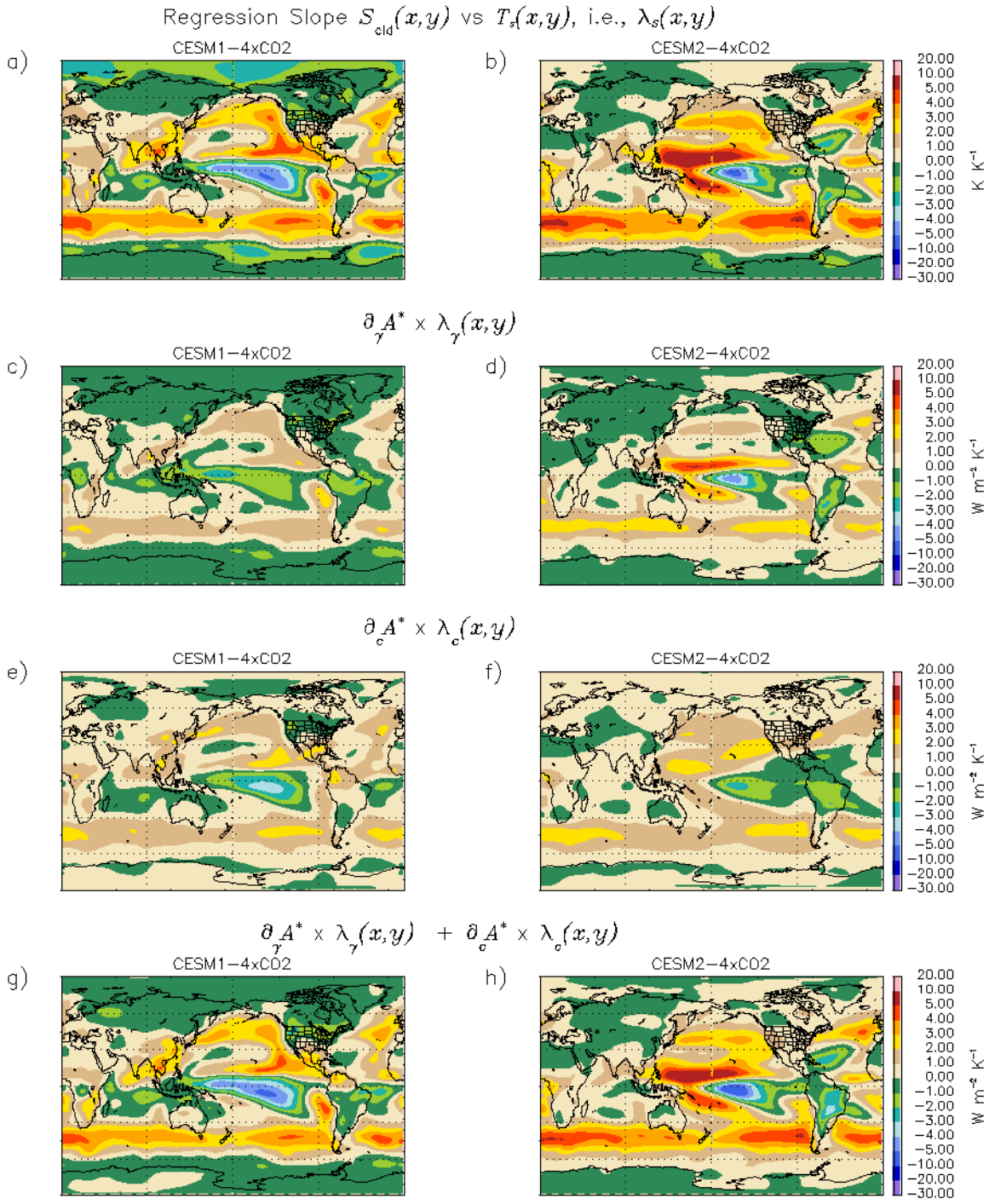

Figure 12. Cloud-related shortwave feedbacks as functions of latitude and longitude over years 100-800 of CESM1-4xCO2 and CESM2-4xCO2: **a, b)** Linear regression slopes for shortwave CRE $\mathcal{S}_{cld}$ vs. T, i.e., $\lambda_{\mathcal{S}_{cld}}$. **c, d)** Cloud scattering contribution $\Lambda_{\gamma_{cld}}$ (Eq. 11b) to shortwave feedback. **e, f)** Cloud amount contribution Λ_c (Eq. 11a) to shortwave feedback. **g, h)** Sum of $\Lambda_{\gamma_{cld}}$ and Λ_c. Left column (**a, c, e, g**) shows results for CESM1-4xCO2 and right column (**b, d, f, h**) shows results for CESM2-4xCO2.

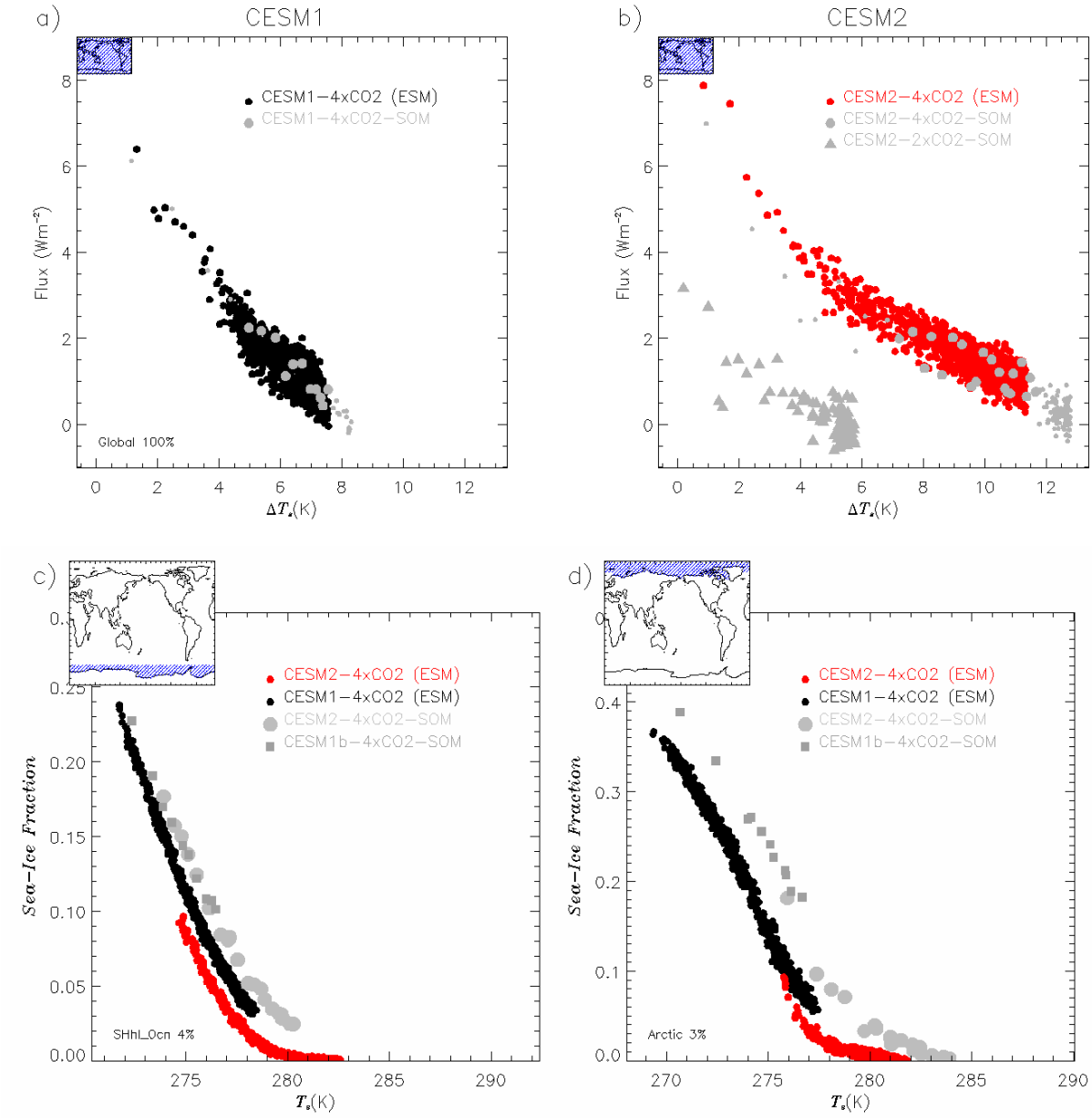

Figure 13. Top panels (**a, b**) show $\overline{N}$, net annual-mean global radiative imbalance at TOM, as a function of global mean surface temperature change $\Delta\overline{T}$ for fully-coupled (ESM) and slab-ocean (SOM) abrupt CO_2 increase experiments: **a)** CESM1. Gray circles show CESM1b-4xCO2-SOM, and black circles show CESM1-4xCO2 (ESM); and **b)** CESM2. Gray circles show CESM2-4xCO2-SOM, red circles show CESM2-4xCO2 (ESM), and gray triangles in show CESM2-2xCO2-SOM. Larger gray circles in **a** and **b** show years in the SOM 4xCO2 experiments where $\Delta\overline{T}$ overlaps with that in the year 100–800 range of the corresponding ESM experiments, i.e., years 5–15 of CESM1-4xCO2-SOM and years 10–30 of CESM2-4xCO2-SOM. Bottom panels (**c, d**) show sea ice fraction as a function of regional mean surface temperature: **c)** High-latitude Southern Ocean; and **d)** Arctic. Sea ice fraction in years 100–800 in CESM1-4xCO2 (ESM) and CESM2-4xCO2 (ESM) is shown, along with years 5–15 for CESM1b-4xCO2-SOM and years 10–30 for CESM2-4xCO2-SOM.

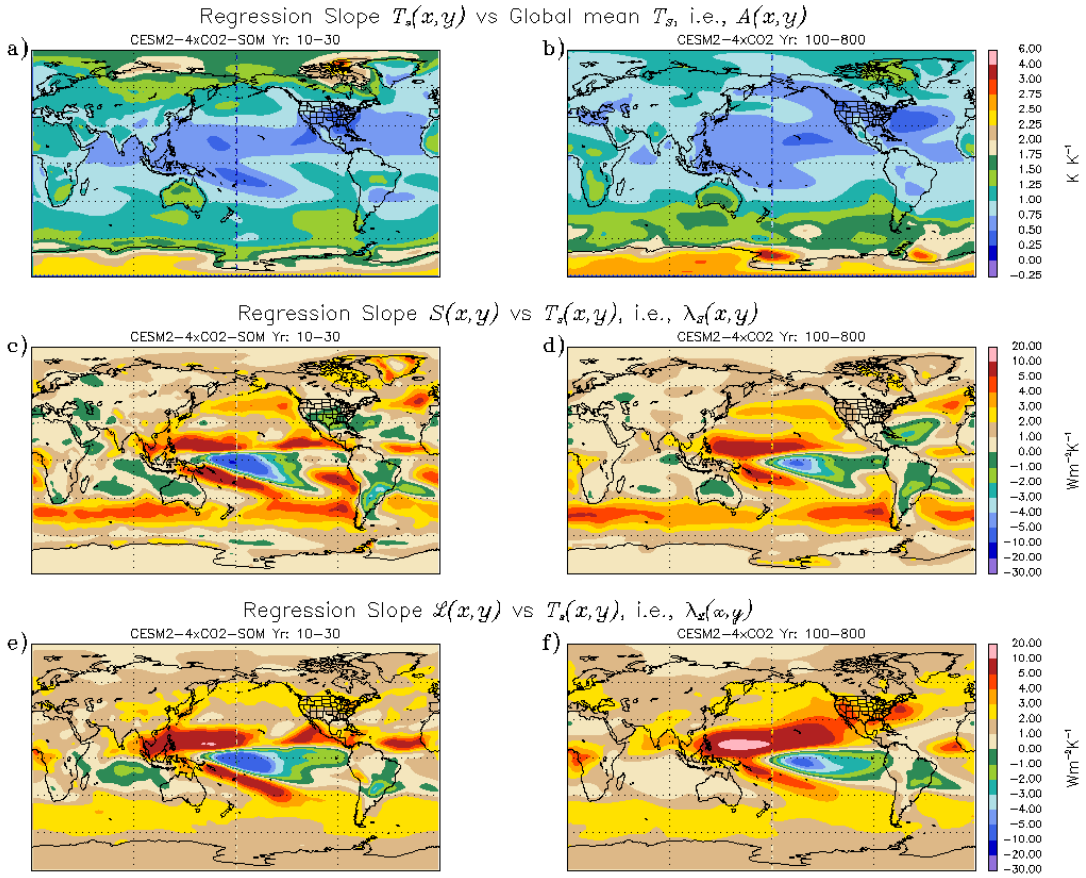

Figure 14. Slopes from linear regressions as functions of latitude and longitude for CESM2-4xCO2-SOM (**a**, **c**, **e**) and CESM2-4xCO2 (**b**, **d**, **f**): **a**, **b)** $A(x, y)$, the local warming amplification factor from regression of local temperature versus global mean temperature $\overline{T}$; **c**, **d)** $\lambda_{\mathcal{S}}(x, y)$, the local shortwave feedback from regression of shortwave radiation $\mathcal{S}$ versus local temperature; and **e**, **f)** $\lambda_{\mathcal{L}}(x, y)$, the local longwave feedback from regression of shortwave radiation $\mathcal{S}$ versus local temperature. Regressions are performed over years 10–30 for CESM2-4xCO2-SOM and years 100–800 for CESM2-4xCO2 (ESM).

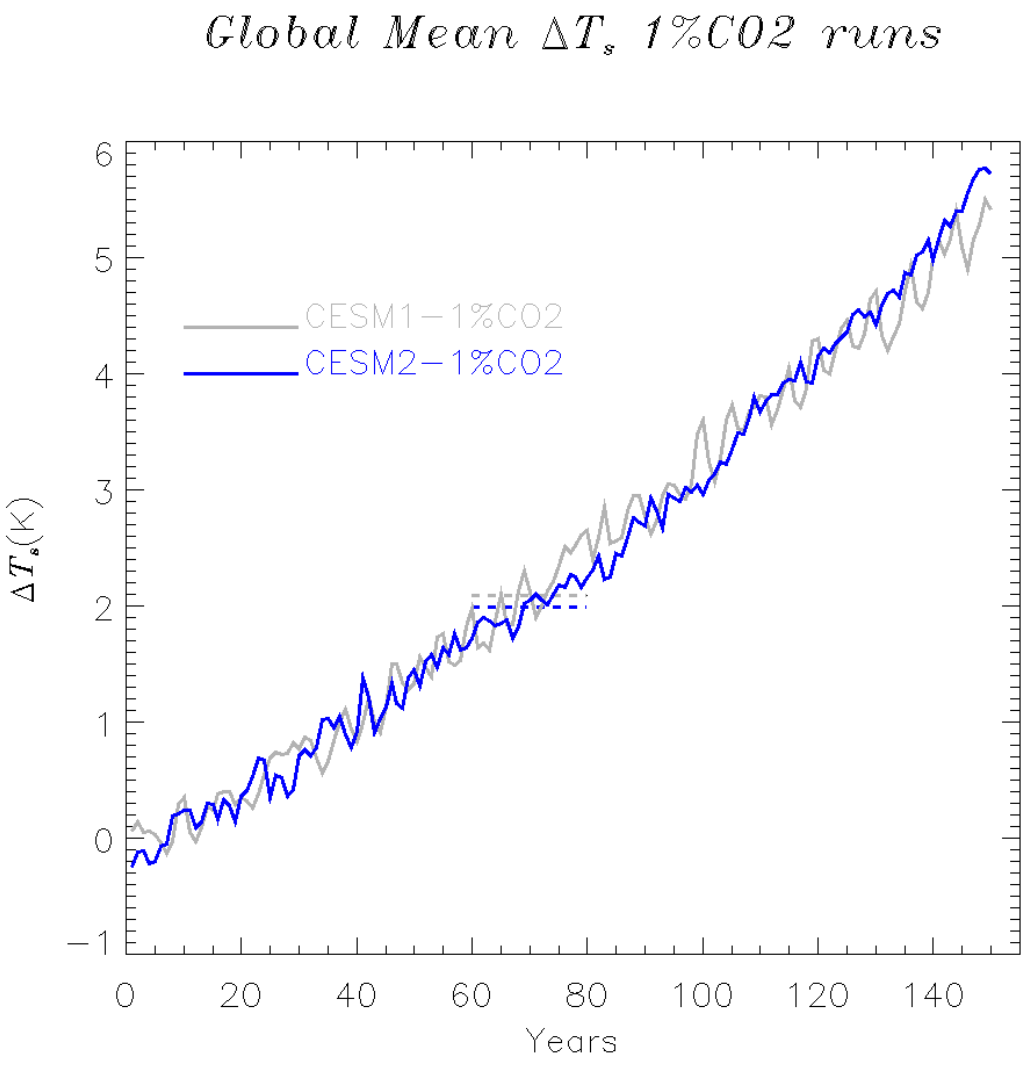

Figure 15. Warming $\Delta\overline{T}_{1\%}$ (Appendix A) as a function of time for 1%CO2 experiments using CESM1 (gray) and CESM2 (blue). Dashed lines for years 60–80 indicate transient climate sensitivity (TCR) values for CESM1 (2.1K) and CESM2 (2.0K). TCR is defined as the mean of $\Delta\overline{T}_{1\%}$ over years 60–80 in the 1%CO2 scenario.

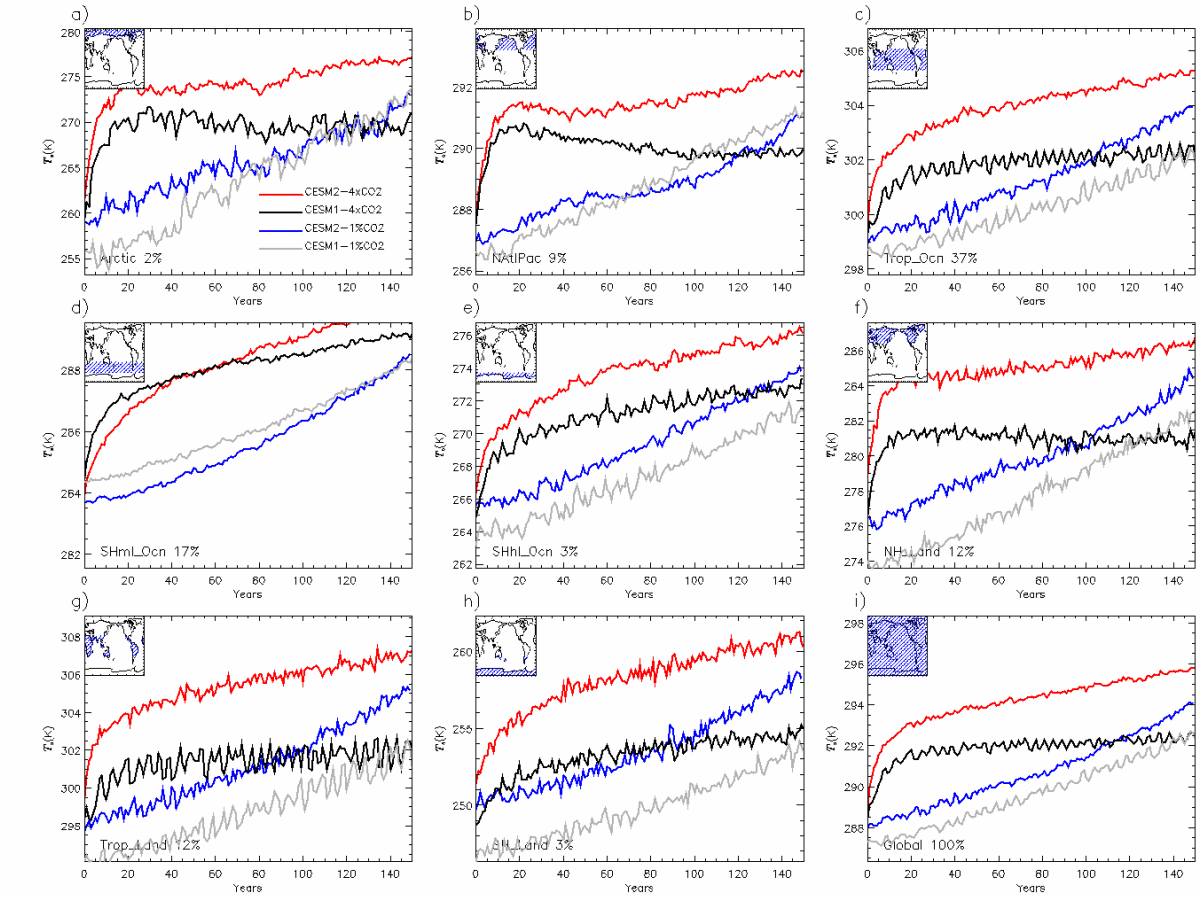

Figure 16. Regional annual-mean surface temperature T_k as a function of time for analysis regions in Fig. 5; CESM1-1%CO2 (gray), CESM2-1%CO2 (blue), CESM1-4xCO2 (black), and CESM2-4xCO2 (red).

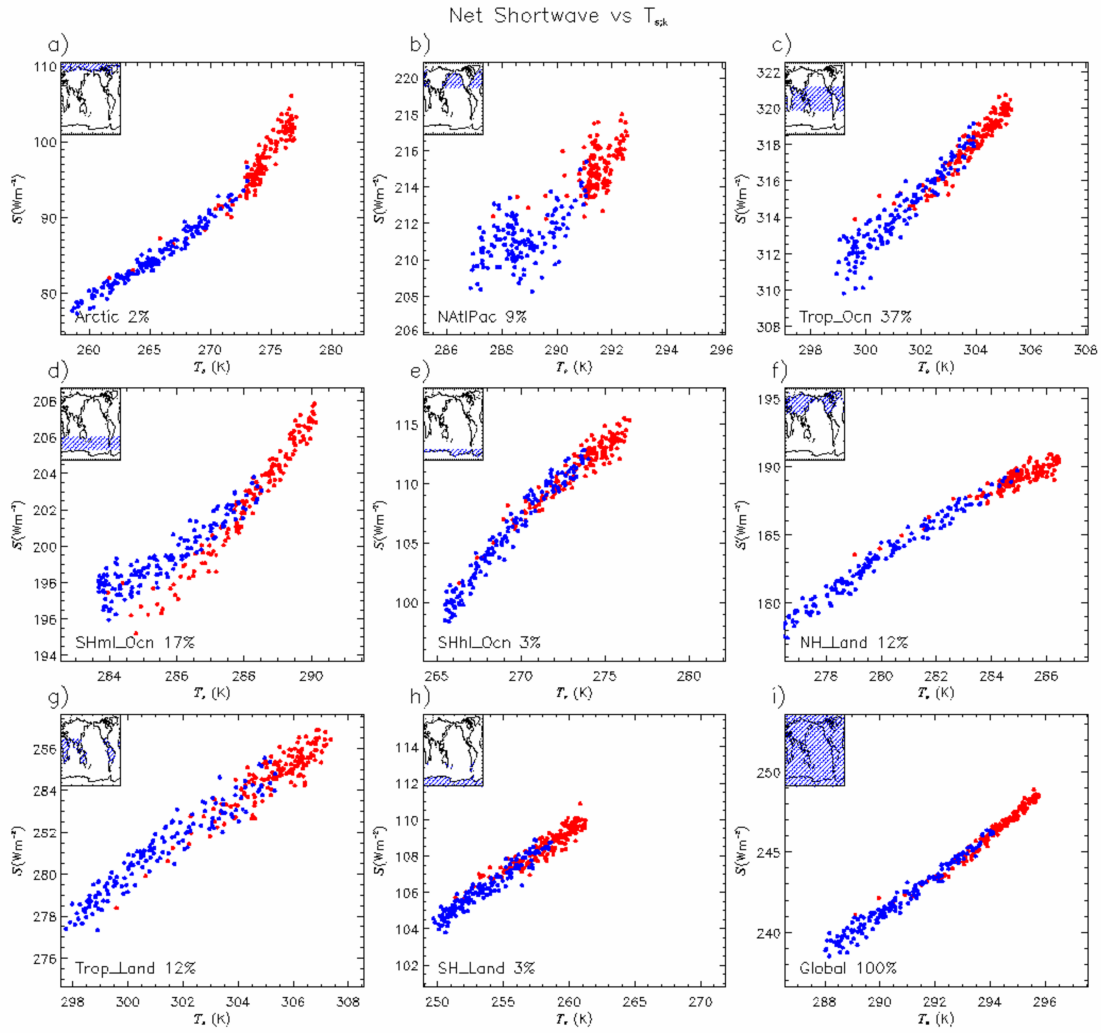

Figure 17. Regional, annual-mean TOM shortwave radiation $\mathcal{S}_k$ as a function of mean surface temperature T_k for regions in Fig. 5; CESM2-4xCO2 (red circles) and CESM2-1%CO2 (blue circles). The plots show results for years 1–150 of both experiments.

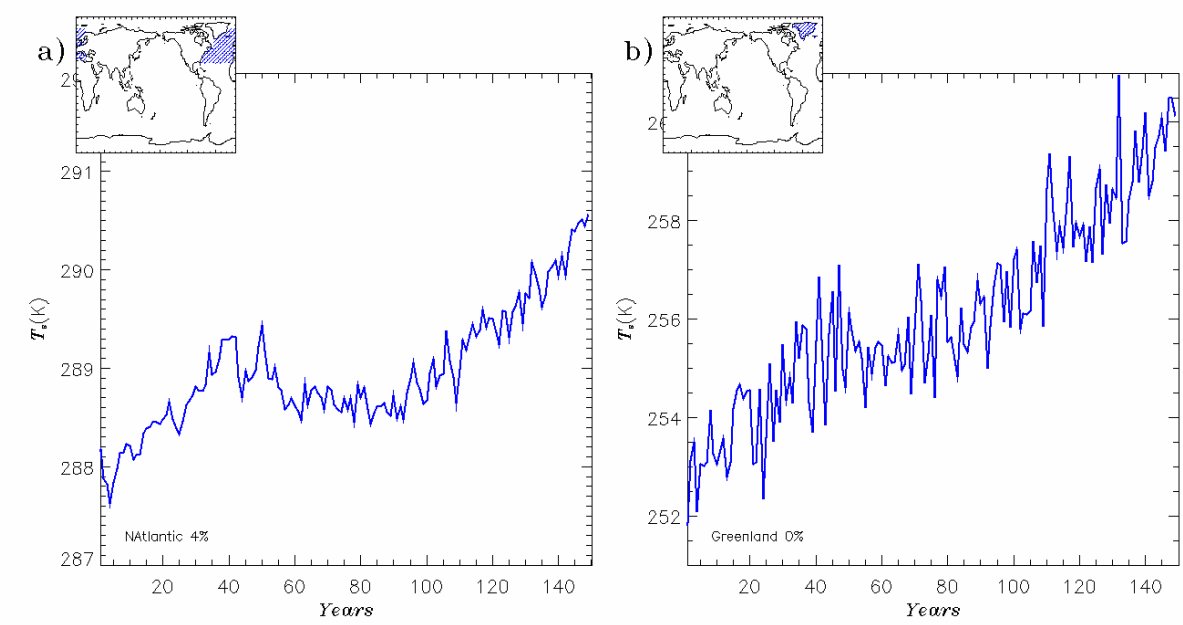

Figure 18. Regional mean surface temperature T_k as a function of time in the CESM2-1%CO2 experiment: **a)** North Atlantic; **b)** Greenland. The respective regions are shown in the panel insets.

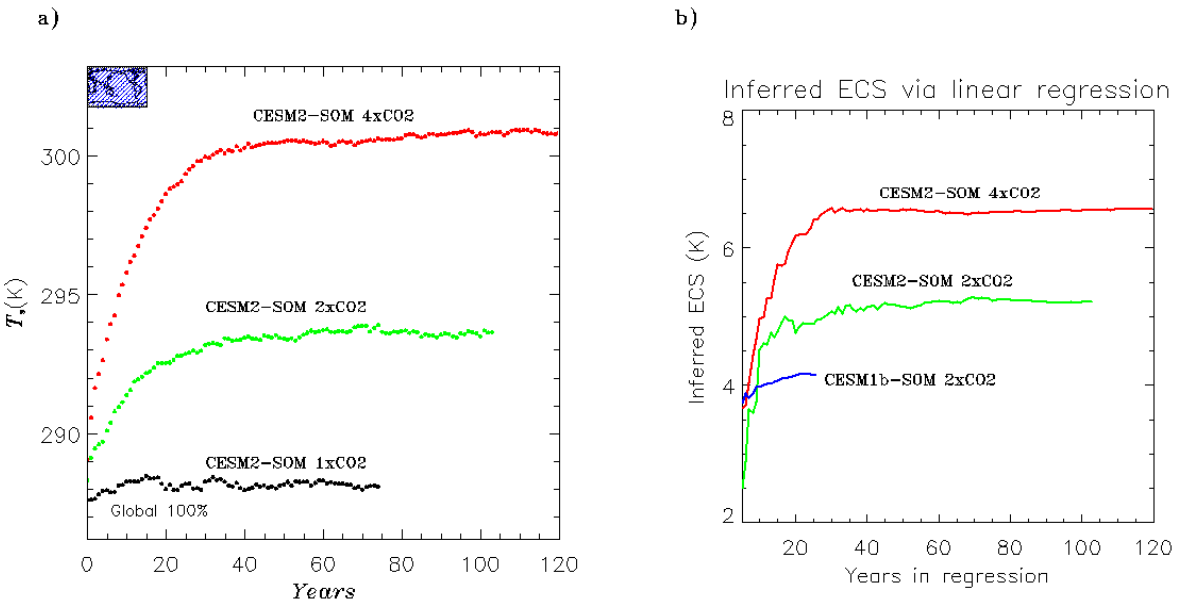

Figure A1. **a)** Time series of $\overline{T}$ from SOM integrations. **b)** Inferred iECS derived from SOM runs.